Angular Effect of Undetected Clouds in Infrared Window Radiance Observations: Aircraft Experimental Analyses

NICHOLAS R. NALLI

I.M. Systems Group, Inc., Rockville, Maryland

WILLIAM L. SMITH

Hampton University, Hampton, Virginia

QUANHUA LIU

NOAA/NESDIS/Center for Satellite Applications and Research, College Park, Maryland

(Manuscript received 2 September 2015, in final form 12 February 2016)

ABSTRACT

This paper furthers previous investigations into the zenith angular effect of cloud contamination within infrared (IR) window radiance observations commonly used in the retrieval of environmental data records (EDRs). Here analyses were performed of clear-sky forward radiance calculations versus observations obtained under clear to partly cloudy conditions over ocean. The authors utilized high-resolution IR spectra observed by the aircraft-based National Polar-Orbiting Partnership (NPP) Aircraft Sounder Test Bed-Interferometer (NAST-I) during the Joint Airborne Infrared Atmospheric Sounding Interferometer (IASI) Validation Experiment (JAIVEx) and performed forward calculations using collocated dropsondes. An aerosol optical depth EDR product derived from Geostationary Operational Environmental Satellite (GOES) was then applied to detect clouds within NAST-I fields of view (FOVs). To calculate the angular variation of clouds, expressions were derived for estimating cloud aspect ratios from visible imagery where cloud shadow lengths can be estimated relative to cloud horizontal diameters. In agreement with sensitivity calculations, it was found that a small cloud fraction within window radiance observations can have a measurable impact on the angular agreement with clear-sky calculations on the order of 0.1–0.4 K in brightness temperature. It was also found that systematic sun-glint contamination can likewise have an impact on the order of 0.1 K. These results are germane to IR sensor data record (SDR) calibration/validation and EDR retrieval schemes depending upon clear-sky SDRs, as well as radiative transfer modeling involving randomly distributed broken cloud fields.

1. Introduction

As discussed previously in Nalli et al. (2012, 2013a), accurate satellite observations (obs) and calculations (calc) of clear-sky, top-of-atmosphere (TOA) spectral radiances are necessary for retrieval of environmental data records (EDRs) from satellite infrared (IR) sounder and imager remote sensing systems. IR-based EDR physical retrieval algorithms are based upon the minimization of clear-sky obs minus calc (obs − calc, or equivalently from the forward modeling perspective, calc − obs). Therefore, it is important that differences between observation and calculation be minimal under well-characterized conditions over the range of satellite zenith angles θ. A systematic angular dependence in obs − calc may lead to undesirable scan-dependent artifacts and/or errors in the calibration/validation (cal/val) of sensor data records (SDRs) and, consequently, EDRs. Current satellite-based IR sounding systems are based upon the measurement of onboard-calibrated high-spectral-resolution radiances on the order of thousands of channels over the IR spectrum (i.e., "hyperspectral" radiances) (e.g., Smith et al. 2009) and include the Joint Polar Satellite System (JPSS) Cross-Track Infrared Sounder (CrIS) on board the *Suomi–National Polar-Orbiting Partnership* (*SNPP*) satellite (Goldberg et al. 2013), the

Corresponding author address: Nicholas R. Nalli, NOAA/NESDIS/Center for Satellite Applications and Research (STAR), NCWCP E/RA2, 5830 University Research Court #2841, College Park, MD 20740-3818.
E-mail: nick.nalli@noaa.gov

DOI: 10.1175/JAS-D-15-0262.1

MetOp Infrared Atmospheric Sounding Interferometer (IASI) (Cayla 1993; Hilton et al. 2012) and the *Aqua* Atmospheric Infrared Sounder (AIRS) (Chahine et al. 2006). Because water-droplet clouds are typically opaque in the IR spectrum, EDR retrievals must assume some degree of cloud-free radiative transfer within the sensor field of view (FOV) or field of regard (FOR). In the case of sounding systems, radiances from microwave (MW) sounders—for example, the Advanced Technology Microwave Sounder (ATMS) on board *SNPP* (Weng et al. 2012)—are utilized to ''cloud clear'' the IR spectra within partly cloudy FORs (e.g., Susskind et al. 2003). In the case of narrowband imager systems, a ''cloud-mask'' algorithm is applied (e.g., Thomas et al. 2004), using radiances from IR channels, as well as solar-spectrum [or ''visible'' (VIS)] channels over sunlit portions of Earth (i.e., IR/VIS), to screen cloudy FOVs. The remaining ''clear sky'' FOVs can then be used for EDR retrievals—for example, global sea surface temperature (SST) and aerosol optical depth (AOD).

As discussed in Nalli et al. (2012, 2013a), a fundamental problem in clear-sky calc − obs analyses is the assumption of pure global clear-sky observations, when in reality we only have access to observations obtained from either cloud-clearing (in the case of IR/MW sounder systems) or cloud-masking (in the case of IR/VIS imager systems) algorithms as mentioned above. Because of this, clear-sky radiance products (i.e., clear-sky obs) will be subject to algorithmic errors, something commonly referred to as ''cloud contamination.'' Generally speaking, a small degree of residual clouds (e.g., subpixel clouds) and aerosols can remain in clear-sky radiances regardless of the algorithm used. This may lead to an observation that is cold-biased relative to a clear-sky calculation for channels sensitive to tropospheric layers below the cloud top (e.g., Benner and Curry 1998; Nalli and Stowe 2002; Sokolik 2002; Maddy et al. 2011; Nalli et al. 2012). Furthermore, global environmental satellite observations are obtained from sensors that scan Earth at oblique local zenith angles θ, and it is well established that apparent cloud cover increases with angle owing to the decrease in probability of clear (cloud free) lines of sight (PCLoS) (e.g., Kauth and Penquite 1967; Lund and Shanklin 1972, 1973). Subpixel cloud contamination in an ensemble of observations (e.g., arising from false negatives in the cloud-mask result) may thus have angular dependence, assuming the occurrence of false negatives does not vary appreciably with view geometry. To quantify IR brightness temperature sensitivity to angularly varying cloud contamination, Nalli et al. (2012) derived simple models for idealized ''superwindow'' channels assuming that the angular variation in probability for cloud contamination on average would behave inversely as PCLoS for a very small absolute cloud fraction (which is similar to assuming the cloud-mask algorithm has a small, angularly independent fraction of false negatives in regions consisting of broken, subpixel clouds with small absolute cloud fractions). Aerosol contamination was also assumed to behave according to the increased slant path arising from a small AOD. It was found that very small levels of contamination can theoretically lead to measurable angular effects with a ''concave up'' signal in calc − obs brightness temperatures[1] on the order of hundreds of millikelvins or more (cf. Nalli et al. 2012). In the follow-up companion paper (i.e., Nalli et al. 2013a), analyses of satellite hyperspectral sounder and narrowband imager systems were conducted. Based on the sounder cloud-cleared radiances (CCRs) and collocated radiosonde observations (RAOBs), calc − obs analyses were performed that showed a possible impact of clouds on the systematic error (bias) of sounder temperature EDR retrievals near the surface on the order of $\simeq -1$ to -3 K. Wong et al. (2015) have since confirmed cloud contamination biases in lower-troposphere temperature profile EDRs (AIRS version 6) of approximately -2 K based on a thorough analysis against global RAOBs and Moderate Resolution Imaging Spectroradiometer (MODIS) cloud pressure and optical depth estimates.

In the current work we examine the potential cloud impact on the angular distribution of IR calc − obs using hyperspectral radiance observations obtained from aircraft overflying clear-to-partly-cloudy atmospheric conditions during an ocean-based validation field experiment. We conduct analyses of microwindow calc − obs as a function of sensor zenith angle based on these observations along with concurrent dropsonde observations. The observations were originally intended to be clear sky for the purposes of satellite IR sounder cal/val, but low-level microscale clouds had subsequently formed during the observing period. Because the clouds were difficult to detect in satellite imagery, we realized that the dataset provided sample conditions under which satellite radiance observations may be cloud contaminated. Unlike satellite-based cloud-cleared sounder data, the aircraft-based spectral data are at a high spatial resolution comparable to satellite imager data, with high spectral resolution to allow for careful selection of channels to minimize the impacts of absorbing gas uncertainties in the forward calculation (e.g., Nalli and Smith 2003).

[1] As in our previous papers, we use the term ''concave up'' to describe an increasing positive bias in calc − obs with $|\theta|$ symmetric from $\theta = 0°$.

2. Radiative transfer model

This section overviews the radiative transfer model (RTM) used for high-spectral-resolution quasimonochromatic radiance calculations valid for ocean surfaces considered by this work.

a. Microwindow channel selection

To minimize uncertainties arising from gas absorption deviating from atmospheric state parameter inputs (including errors in raob-measured H_2O, as well as assumed values for fixed gases), we carefully selected six spectral microwindows (i.e., spectral regions of high transmittance located between absorption lines) minimally impacted by absorbing species in the longwave IR (LWIR) region roughly spanning 650–1200 cm^{-1} [cf. Nalli and Smith (2003), their Fig. 1]. Although there are more transparent microwindows in the shortwave IR (SWIR) region (roughly spanning 2000–2700 cm^{-1} and largely due to minimized H_2O continuum absorption) the use of daytime data containing sun glint correlated with zenith view angle precluded any possible exploitation of such channels, even with the sun-glint estimation detailed in appendix A.

The peak of the LWIR H_2O continuum transmittance is located on the SWIR side of the O_3 band (i.e., ≃1080–1200 cm^{-1}). However, for a sensor located at high altitudes it is desirable to avoid the O_3 band as much as possible. For satellite sounder analyses, Nalli et al. (2013a) utilized LWIR microwindow channels located just outside of this region to minimize trace gas and H_2O continuum uncertainty for a sensor located at the TOA, defined by ν = [956.5, 958.5], [962.5, 964.5], and [1202.0, 1204.5] cm^{-1}. They found reduced sensitivity in TOA calc − obs to nominal systematic errors in various input state parameters (e.g., H_2O, CO_2, and O_3) in these hyperspectral microwindows compared to narrowband Advanced Very High Resolution Radiometer (AVHRR) channels [cf. Fig. 1 of Nalli et al. (2013a)], as would be expected. In the current work, for an aircraft-based spectrometer (discussed in section 3a), to diminish the impact of the sun-glint contamination (and further avoid the proximity of trace gas absorption lines), we replaced the [1202. 0, 1204.5] cm^{-1} microwindow with ν = [899.5, 901.8] cm^{-1}. Given the high-spectral-resolution, quasimonochromatic datasets used in this work (described in section 2d for calc and section 3a for obs), we simply performed boxcar averages for the spectral limits indicated for computing calc − obs for these microwindows (discussed in section 3c).

b. IR radiative transfer equation

The forward radiance calculation for a downlooking sensor operating in an IR window channel located at or near the TOA consists primarily of the surface-leaving radiance (SLR) transmitted through the atmosphere along with the upwelling emission of the atmosphere. The SLR, which consists of sea surface emission (emissivity and skin temperature) and quasi-specular reflection of downwelling atmospheric and solar radiance, is the dominant term within window channels (discussed in more detail in section 2c). Because liquid-phase clouds are generally nontransmissive in the IR, radiative transfer in window channels from the surface through the entire atmosphere can only occur within clear-sky (cloud free) paths. Scattering due to aerosols is usually of second order, and thus a nonscattering (i.e., aerosol free), azimuthally symmetric atmosphere is also often assumed. The clear-sky IR monochromatic radiative transfer equation (RTE) for a downlooking sensor located at atmospheric pressure p_0 observing the surface at local zenith θ and azimuth ϕ angles of the sensor FOV is then given by

$$R_\nu(p_0,\theta,\phi) = I_\nu(p_s,\theta,\phi)\mathscr{T}_\nu(p_s,\theta,X) + \int_{p_s}^{p_0} B_\nu[T(p)]\frac{\partial\mathscr{T}_\nu(p,\theta,X)}{\partial p}dp, \quad (1)$$

where $R_\nu(p_0, \theta, \phi)$ is the radiance measured by the sensor at wavenumber ν (typically measured in mW m^{-2} sr^{-1} cm^{-1}), $I_\nu(p_s, \theta, \phi)$ is the spectral upwelling SLR (intensity) at surface pressure p_s [defined by Eq. (2) in section 2c], $\mathscr{T}_\nu(p, \theta, X)$ is the pressure-to-observer (from p to p_0) path transmittance for atmospheric state vector X, $\partial\mathscr{T}_\nu(p, \theta, X)/\partial p$ is the weighting function, and B_ν is the Planck blackbody function for atmospheric layer temperature $T(p)$; the second term on the right constitutes the integrated upwelling atmospheric-emitted radiance. It is assumed that the monochromatic approximation is valid for the quasimonochromatic atmospheric transmittance and radiance forward model calculations described in section 2d.

c. SLR

For a downlooking sensor located just above the surface at pressure p_s operating in an atmospheric spectral microwindow, SLR is given by

$$I_\nu(p_s,\theta,\phi) = \varepsilon_\nu(\theta,\phi)B_\nu(T_s) + \int_0^{2\pi}\int_0^{\pi/2} r_\nu(\theta',\theta;\phi',\phi)[I_\nu^{\downarrow}(p_s,\theta') + I_{\nu\odot}^{\downarrow}(p_s,\theta',\phi')]\cos(\theta')\sin(\theta')\,d\theta'\,d\phi', \quad (2)$$

where T_s is the surface skin temperature, $\varepsilon_\nu(\theta, \phi)$ is the surface IR emissivity, $r_\nu(\theta', \theta; \phi', \phi)$ is the bidirectional reflectance function describing the reflectance of incident rays at zenith and azimuth angles (θ', ϕ') into the sensor

FOV (θ, ϕ) [e.g., Thomas and Stamnes (1999), p. 134], and $I^{\downarrow}_{\nu\odot}(p_s, \theta', \phi')$ and $I^{\downarrow}_{\nu}(p_s, \theta')$ are the solar and atmospheric downwelling radiances at the surface, the latter defined (again, assuming azimuthal symmetry) by

$$I^{\downarrow}_{\nu}(p_s,\theta') \equiv \int_0^{p_s} B_{\nu}[T(p)]\,\frac{\partial \mathcal{T}_{\nu}(p,\theta',X)}{\partial p}\,dp. \qquad (3)$$

Unlike our previous paper (Nalli et al. 2013a), in this paper we include the reflected solar contribution (i.e., sun glint) in Eq. (2). Although sun glint is not typically considered problematic in the LWIR, it can sometimes have a nonnegligible magnitude (e.g., Závody and Birks 2004; Yao et al. 2012), which can be important under the daytime circumstances inherent in the dataset used in this work and described in section 3. In the literature (e.g., Goody and Yung 1989; Bréon and Henriot 2006; Kay et al. 2009; Merchant et al. 2009; Zhang and Wang 2010; Jackson and Alpers 2010) we find that the solar term in Eq. (2) is typically approximated as $r_{\nu}(\theta_{\odot}, \theta; \phi_{\odot}, \phi)L^{\downarrow}_{\nu\odot}(p_s, \theta_{\odot})$ (see appendix A for derivation), which is called the sun-glint radiance and defined as the reflected downwelling solar radiance $L^{\downarrow}_{\nu\odot}(p_s, \theta_{\odot})$ into the sensor FOV (Goody and Yung 1989; Merchant et al. 2009). Note that $L^{\downarrow}_{\nu\odot}(p_s, \theta_{\odot})$ varies with the solar zenith angle $\theta_{\odot}$ only because of the transmittance term (see appendix A). This approximation simplifies Eq. (2) as

$$I_{\nu}(p_s,\theta,\phi) = \varepsilon_{\nu}(\theta)B_{\nu}(T_s) + \int_0^{2\pi}\int_0^{\pi/2} r_{\nu}(\theta',\theta;\phi',\phi)I^{\downarrow}_{\nu}(p_s,\theta')\cos\theta'\sin\theta'\,d\theta'\,d\phi' + r_{\nu}(\theta_{\odot},\theta;\phi_{\odot},\phi)L^{\downarrow}_{\nu\odot}(p_s,\theta_{\odot}). \qquad (4)$$

For details on calculating the sun-glint bidirectional reflectance $r_{\nu}(\theta_{\odot}, \theta; \phi_{\odot}, \phi)$ and solar luminosity $L^{\downarrow}_{\nu\odot}(p_s, \theta_{\odot})$, the reader is referred to appendix A.

Full calculation of the remaining hemispheric IR water-reflected downwelling atmospheric radiance term in Eq. (4) (the second term on the right-hand side) is usually impractical (involving a double integral of downwelling atmospheric radiances and transmittances), so additional simplification is sought. Given that the ocean surface behaves as a quasi-specular reflector (see appendix A for more discussion on this), a dominant specular component is found in the reflected radiation field (Stephens 1994; Nalli et al. 2001; Martin 2004). Thus, for ocean surfaces it is typical practice to ignore nonspecular contributions; that is, $r_{\nu}(\theta', \theta; \phi', \phi)I^{\downarrow}_{\nu}(p_s, \theta') = 0$ for $\theta' \neq \theta \vee \phi' \neq \phi$, and thus $r_{\nu}(\theta', \theta; \phi', \phi)\delta(\theta' - \theta)\delta(\phi' - \phi)I^{\downarrow}_{\nu}(p_s, \theta')$, where the δ-product here designates the two-dimensional Dirac delta function. The IR surface emission and atmospheric reflection terms thus simplify as

$$\begin{aligned}&\varepsilon_{\nu}(\theta)B_{\nu}(T_s) + \int_0^{2\pi}\int_0^{\pi/2} r_{\nu}(\theta',\theta;\phi',\phi)\delta(\theta'-\theta)\delta(\phi'-\phi)I^{\downarrow}_{\nu}(p_s,\theta')\cos\theta'\sin\theta'\,d\theta'\,d\phi' \\ &= \varepsilon_{\nu}(\theta)B_{\nu}(T_s) + r_{\nu}(\theta,\theta;\phi,\phi)I^{\downarrow}_{\nu}(p_s,\theta) = \varepsilon_{\nu}(\theta)B_{\nu}(T_s) + [1-\varepsilon_{\nu}(\theta)]I^{\downarrow}_{\nu}(p_s,\theta), \qquad (5)\end{aligned}$$

where the last step is a consequence of energy conservation at the surface (assuming zero transmittance), and it is recognized that dependence upon azimuth angle has been eliminated.

Equation (5) now requires only specification of T_s and $I^{\downarrow}_{\nu}(p_s, \theta)$ and sea surface emissivity $\varepsilon_{\nu}(\theta)$ at the single zenith view angle θ. The downwelling atmospheric radiance, $I^{\downarrow}_{\nu}(p_s, \theta)$, can be accurately calculated using a transmittance model (see section 2d) given a concurrent temperature and water vapor sounding (e.g., from a radiosonde or dropsonde). Likewise, the emissivity ε_{ν} can be calculated using published models (e.g., Wu and Smith 1997; Masuda 2006; Nalli et al. 2008b). These models typically compute the FOV-mean surface emissivity as a function of mean surface wind speed $\overline{u}$ and zenith emission angle θ, which we designate $\overline{\varepsilon}_{\nu}(\theta, \overline{u})$, and SLR [Eq. (4)] is finally reduced to

$$\begin{aligned}I_{\nu}(p_s,\theta) \approx{}& \overline{\varepsilon}_{\nu}(\theta,\overline{u})B_{\nu}(T_s) + [1-\overline{\varepsilon}_{\nu}(\theta,\overline{u})]I^{\downarrow}_{\nu}(p_s,\theta) \\ &+ r_{\nu}(\theta_{\odot},\theta;\phi_{\odot},\phi)L^{\downarrow}_{\nu\odot}(p_s,\theta_{\odot}), \qquad (6)\end{aligned}$$

which may be substituted back into RTE [Eq. (1)] to calculate $R_{\nu} = R_{\nu}(p_0, \theta)$.

In this paper we employ the "effective emissivity" model (Nalli et al. 2008b,a) that was developed to be used in conjunction with the reflection approximation [Eq. (5)] and has since been implemented within the Community Radiative Transfer Model (CRTM).[2] For

[2] The CRTM was developed at the Joint Center for Satellite Data Assimilation (JCSDA) in the United States in support of satellite radiance assimilation for numerical weather prediction (NWP), satellite product retrievals, and radiance validation for satellite programs including JPSS (Liu and Boukabara 2014).

theoretical details on the sea surface emissivity model, the reader is referred to Nalli et al. (2001, 2008b,a) and references therein.

d. Atmospheric transmittance and radiance model

To ensure accurate high-spectral-resolution forward radiance calculations using Eq. (1) (i.e., calc), quasimonochromatic atmospheric transmittances $\mathscr{T}_\nu(p, \theta, X)$, and column-integrated radiances were rigorously calculated using the Atmospheric and Environmental Research, Inc. (AER) Line-By-Line Radiative Transfer Model (LBLRTM) (Clough et al. 2005), version 12.2, with the MT_CKD v2.5.2 continuum model. Given accurate atmospheric state parameters X (viz., profiles of temperature, water vapor, and secondary absorbing gases), the variation of clear-sky slant-path transmittances based upon model physics is generally considered to be highly accurate. The LBLRTM calculations performed in this work take into account absorbing species relevant to the spectral microwindows defined in section 2a—namely, H_2O, CO_2, O_3, N_2O, CH_4, CFC-11, CFC-12, and CCl_4. Fixed gas inputs to LBLRTM are uniform mixed CO_2 set to the 2008 global levels (384.8 ppm) (Arndt et al. 2010) and CFCs as provided by LBLRTM.

For the upwelling transmittance and radiance calculation at the observer level, LBLRTM takes Earth curvature into account given the sensor-referenced view zenith angle at the observer height, which is the supplement of the sensor-referenced view nadir angle ϑ (i.e., the sensor scan angle)—that is, $\pi - \vartheta$. However, the downwelling radiance calculation at the surface (the LBLRTM "observer" at the surface looking up) $I_\nu^\downarrow(p_s)$ must be at the surface incident zenith angle, which is equal to the satellite zenith angle θ, which can be calculated using the law of sines,

$$\theta = \arcsin\left[\frac{r_e + z_0}{r_e}\sin(|\vartheta|)\right], \tag{7}$$

where r_e is the mean Earth radius and z_0 is the sensor height. In the current work (section 3a), $z_0 \simeq 17$ km and $|\vartheta| < 45°$ implies $|\theta - \vartheta| \lesssim 0.3°$.

3. Aircraft campaign IR microwindow analysis

In an effort to examine more closely the cloud/aerosol angular impact on radiance observations independent of a cloud-clearing or cloud-mask algorithm, we turned to field campaign data that include radiance spectra obtained from an aircraft-based Fourier transform spectrometer (FTS). Specifically, we used data obtained from the Joint Airborne IASI Validation Experiment (JAIVEx) (Newman et al. 2012) during the 29 April 2007 clear-sky overflight of the Gulf of Mexico (e.g., Larar et al. 2010). Ocean-based campaigns such as this provide the tightest control on the lower-boundary (surface) radiometric variables (e.g., Nalli et al. 2006).

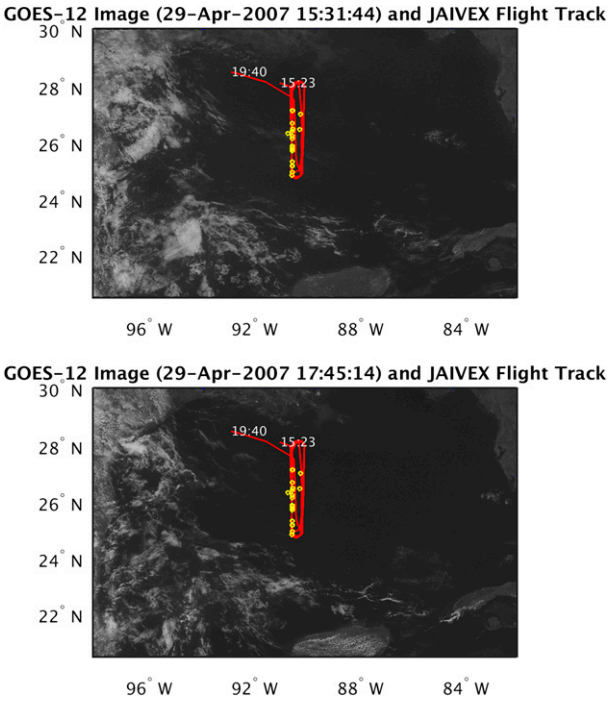

FIG. 1. JAIVEx 29 Apr 2007 WB-57 flight path during the NAST-I sampling period (1523–1940 UTC) overlying concurrent *GOES-12* visible channel (band 1, 0.65 μm) imagery for (top) 1531:44 and (bottom) 1745:14 UTC. Dropsonde launches from the FAAM BAe 146 underflight are shown with yellow circles.

a. Experimental overview

Radiance observations at high spectral resolution (unapodized, 0.25 cm^{-1}) were obtained during JAIVEx from the NPP Atmospheric Sounder Test Bed-Interferometer (NAST-I) (Smith et al. 2005), an FTS system similar to IASI and CrIS, but designed for high-altitude aircraft in support of JPSS sounder risk reduction and cal/val. NAST-I was flown on board the NASA WB-57 aircraft during JAIVEx over the Gulf of Mexico spanning 1523–1940 UTC (0923–1340 LST) on 29 April 2007. The WB-57 flew at altitudes ranging between $z_{ac} \simeq 16$ and 18 km, with a corresponding nadir FOV "footprint" at the surface of approximately 2.08–2.34 km (e.g., Smith et al. 2005), which is comparable to the nadir spatial resolution of satellite imagers such as AVHRR.

Complementing the NAST-I radiances are a total of 20 Vaisala dropsondes that were launched from a Facility for Airborne Atmospheric Measurements (FAAM) BAe 146 aircraft underflying the WB-57 at an altitude of

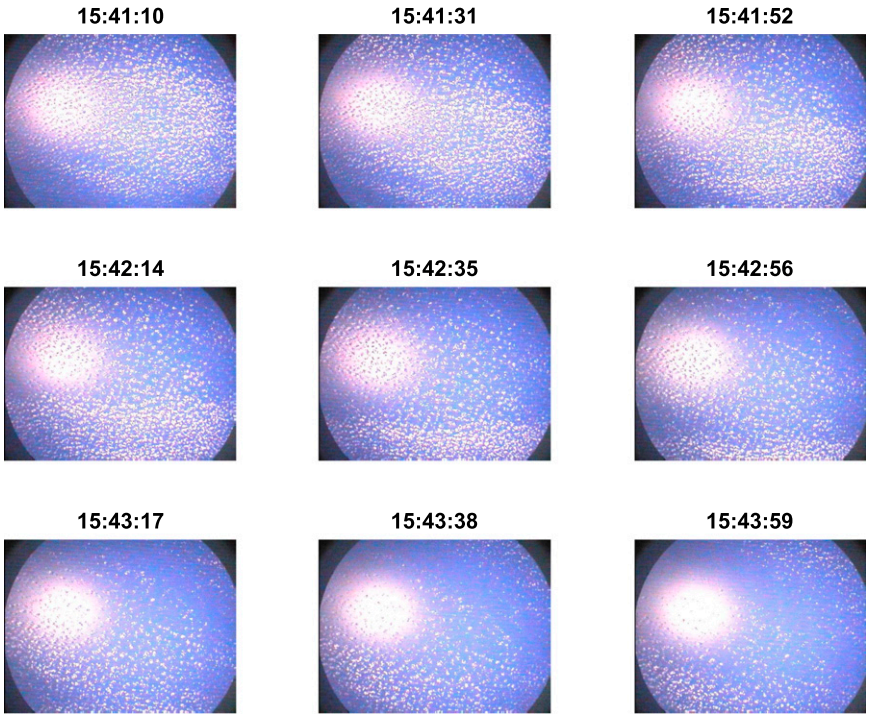

FIG. 2. Sample of time-consecutive images (1541:10–1543:59 UTC) taken from the hemispheric camera mounted on the main fuselage of the WB-57 aircraft during the 29 Apr 2007 JAIVEx overflight of the Gulf of Mexico showing microscale FWC clouds (observed primarily at the south end of the flight track); UTC times estimated from the file time stamps are given for each image.

≃7–8 km. Additionally, a hemispheric camera was mounted on the WB-57 main fuselage for all-sky visible color imagery capable of resolving microscale cloud features spanning the swath scanned by the NAST-I sensor. A total of 712 JPEG images were obtained covering much (but not all) of the NAST-I sampling period, and these were made available to us courtesy of V. Leslie (MIT Lincoln Laboratory). The file time stamp had an undetermined ''offset'' from the actual UTC time (V. Leslie 2010, personal communication). We therefore conducted a careful visual inspection of the images looking for known changes in the aircraft heading (using the NAST-I GPS latitude–longitude and heading data), and using the solar-glint disk (located east-southeast to southeast in the morning, south around noon to south-southwest by early afternoon), we determined the time-stamp offset to be approximately $t(\text{stamp}) \approx t(\text{gps}) + 00{:}32{:}30$. The last image was taken at ≃1840 UTC (1240 LST).

Figure 1 shows the WB-57 flight path and locations of the dropsonde launches during the NAST-I sampling period (1523–1940 UTC) overlying two U.S. National Oceanic and Atmospheric Adminstration (NOAA) Geostationary Operational Environmental Satellite (*GOES-12*) visible channel (band 1, 0.65 μm) images taken within the same time frame. Given that the occurrence of cloud-free FOVs for a IR sounder such as CrIS or IASI is ≲10% (e.g., Maddy et al. 2011), from the vantage point of JAIVEx the GOES imagery gives the appearance of what may be considered nearly ideal clear-sky field conditions throughout the duration of the flight (and, indeed, this particular flight was intended to be just that). However, as seen in Fig. 2, closer examination of the sky conditions using the hemispheric camera reveals the presence of marine boundary layer (MBL) fair weather cumulus clouds (FWC) (e.g., Stull 1985) that were found to be persistent at the mid-to-south end of the flight track. Only a hint of their presence is barely noticeable in the *GOES-12* image (Fig. 1, mainly in the earlier image shown in the top plot). Other images from the all-sky camera (not shown) also reveal the occurrence of thin cirrus observed to be present in an east–west band for several overpasses to the north of the FWC (1618:38–1640:21, 1718:30–1729:20, and 1828:49–1834:25), as well as haze. These images represent the weather conditions observed by sight and reported in the ''flight summary document'' (B. Rieke and J. Bain 2007, unpublished manuscript): ''The sky was clear with very slight haze obscuring the horizon. Near the south end of the track small scattered 'popcorn' cumulus clouds were near the ground in wide bands. Near the

northern end of the track some streaks of cirrus clouds were below and east of the track.'' It thus turns out that the JAIVEx 29 April 2007 overflight actually provides a case of a broken field of subpixel FWC clouds (as well as cirrus and haze) that can elude cloud clearing or cloud masking and be very difficult to clear or mask completely (e.g., Benner and Curry 1998). Finally, unlike low-Earth-orbit satellite data (e.g., *SNPP*, MetOp) taken from successive orbits, the solar-glint disk is systematically present near the center of the FOV of the camera (corresponding to the near-nadir angles of a satellite sensor swath) throughout the observing period.

b. Cloud-cover information from GOES aerosol data

To obtain quantitative characterizations of these MBL FWC (as well as any potential aerosols/haze), we realized that, barring a coregistered imager operating synergistically with the NAST-I on board the aircraft, visible (reflected solar) data acquired from geostationary Earth orbit (GEO) is the best available alternative option. It was also clear that an algorithm designed for detecting very small backscatter signals would be necessary. Recognizing that solar-spectrum-based AOD EDR retrieval algorithms fall into that category, we utilized the GOES Aerosol/Smoke Product (GASP) developed by K. Knapp and collaborators at NESDIS/Center for Satellite Applications and Research (STAR) (Knapp et al. 2002; Prados et al. 2007). The GASP algorithm retrieves total column AOD from GEO orbit by first removing the invariant ''background'' solar reflectance signal using an image composite assembled from the previous month, thereby allowing small transient anomalies (i.e., backscatter due to aerosol, smoke, subpixel cloud) to be detected (Knapp et al. 2002). In essence, the GASP algorithm interprets low-signal, solar-spectrum atmospheric backscattering as AOD.

Figure 3 shows GASP AOD imagery at nominal $4 \times 4\,\mathrm{km}^2$ nadir resolution (Prados et al. 2007) corresponding to the GOES visible channel imagery shown Fig. 1. The AOD distribution was found to span unphysical negative values, so the product distribution was shifted by 0.15 minus the uncorrected mode (which was 0.05), thereby resetting the mode of the distribution to be 0.15, a typical background marine level. It can be seen that the FWC observed by the JAIVEx hemispheric camera appear as intermittent regions of high GASP AOD ($\gtrsim$0.25) in the vicinity of $\simeq$25°–27°N and $\simeq$89°–91°W. In addition, there are more expansive regions of elevated AOD ($\gtrsim$0.15), especially in the earlier image (top plot), that presumably correspond to the haze and/or cirrus reported in the flight summary document. As already posited in this paper, cloud contamination in EDR products such as this is not unusual (Benner and Curry 1998) and is a documented

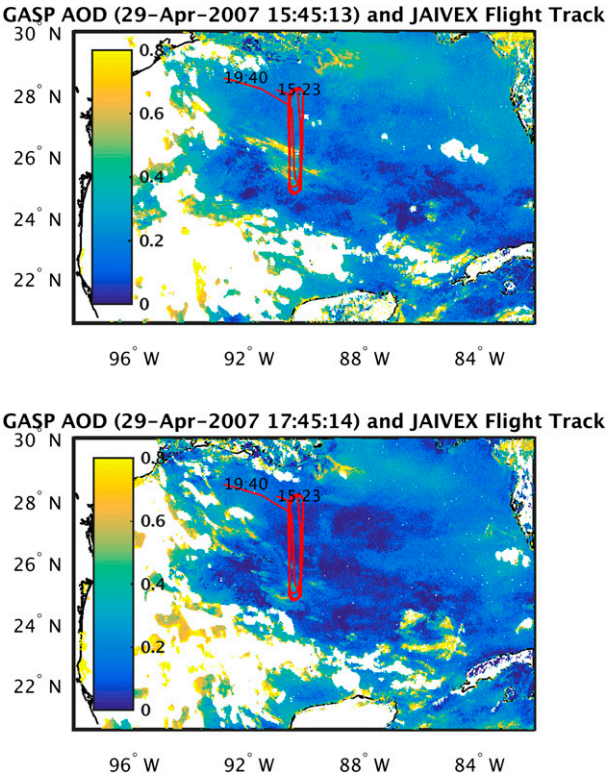

FIG. 3. As in Fig. 1, except showing concurrent GASP (Knapp et al. 2002; Prados et al. 2007) solar-spectrum (visible channel 520–720 nm) AOD retrievals (reduced to $4 \times 4\,\mathrm{km}^2$ resolution) with cloud mask (white areas) for (top) 1545:13 and (bottom) 1745:14 UTC.

artifact found in similar AOD EDR products (e.g., Zhao et al. 2013). However, in our present application this ''contamination'' constitutes the signal to be studied.

In using GOES aerosol data for estimating ''cloudiness'' in the NAST-I FOVs, we first note that a space–time interpolation is necessary. The GASP data are not gridded in geographic coordinates, so we interpolated half-hourly GASP AOD fields (AOD means and standard deviation) to the NAST-I FOV latitude–longitude coordinates. However, the GASP data are derived from the FOVs of the *GOES-12* imager located at (0°N, 75°W). Strictly speaking, the atmospheric paths observed within the GOES FOVs are not the same as those of the NAST-I FOVs given the different vantage points of the two sensors. To account for the different FOVs, we performed a remapping which then enabled the spatial interpolation mentioned above; our method for doing this is detailed in appendix B. The space-interpolated fields were then linearly interpolated in time to the NAST-I GPS times. Figure 4 shows the resulting interpolated values (without cloud masking) along with the evolution of the FWC cloud fields (as well as any aerosol) throughout the aircraft flight duration. The application of these data is described more in section 3e.

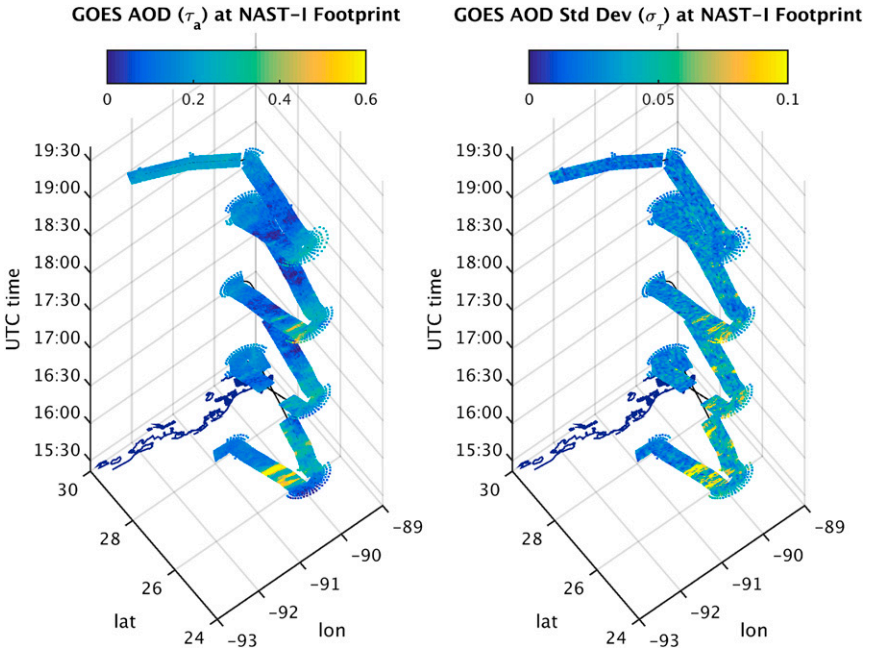

FIG. 4. Three-dimensional space–time interpolations (z axes designating UTC time) of GOES AOD EDR product (GASP) to JAIVEx 29 Apr 2007 NAST-I FOVs: (left) AOD τ_a and (right) AOD standard deviation σ_τ. For geographic reference, the U.S. Gulf Coast is shown at the bottom in blue.

c. *Methodology for computing calc − obs*

We perform calc − obs analyses for the microwindow channels described in section 2a by taking the differences of the calculated and observed brightness temperatures (cf. sections 2b–2d and 3a); that is,

$$\delta T_B(\overline{\nu}, \theta) \equiv \hat{T}_B(\overline{\nu}, \theta) - T_B(\overline{\nu}, \theta), \tag{8}$$

where $\hat{T}_B(\overline{\nu}, \theta)$ and $T_B(\overline{\nu}, \theta)$ are the boxcar averages of quasi-monochromatic values falling within microwindow spectral limits defined in section 2a for calc and obs, respectively. The calc for the individual NAST-I FOVs were conducted based upon a combination of the in situ dropsonde temperature and water vapor profile data along with model outputs from the European Centre for Medium-Range Weather Forecasts (ECMWF) model (1800 UTC analysis, along with the 1200 UTC forecast for 1500 and 2100 UTC). Figure 5 shows skew-T diagrams of the dropsonde temperatures and dewpoints up to 700 hPa, along with the skin SST (MW–IR blended analysis; see below for more on the SST data used) for the cloudy FOVs. For the LBLRTM calculation, dropsonde profile data (temperatures and mixing ratios) $X_0(p_0, x_0, y_0, t_0)$ were first subsampled to the ECMWF model pressure level grid p, spanning 1015–50 hPa (with higher vertical resolution in the lower troposphere). To fill in these soundings at altitudes above the FAAM BAe 146 aircraft flight level (7–8 km), the ECMWF model fields $\tilde{X}$ were linearly interpolated to the dropsonde locations x_0, y_0, and t_0 (which were found to splice quite well with the dropsondes without involving any artificial discontinuities). These combined dropsonde + ECMWF profile "anchor points" $X_0(p, x_0, y_0, t_0)$ were then nearest-neighbor interpolated in space and time to the NAST-I FOV coordinates, yielding $X_0(p, x, y, t)$. However, to account for spatial gradients away from the dropsonde locations, we use the gradients given by the ECMWF model such that $X(p, x, y, t) = X_0(p, x, y, t) + [\tilde{X}(p, x, y, t) - \tilde{X}(p, x_0, y_0, t_0)]$, where X is either T or H_2O, subscript "0" designates dropsonde, and $\tilde{X}$ designate ECMWF profiles linearly interpolated to the FOV (p, x, y, t) and dropsonde (p, x_0, y_0, t_0) locations. Figure 5 shows the mean profiles for cloudy FOVs (determined based upon GASP) along with the derived lifting condensation level (LCL), which is used for estimating cloud dimensions (see below for more on the LCL calculation). For ozone profiles we simply use the ECMWF values linearly interpolated to x, y, and t since there were no ozonesondes.

After employing this procedure for obtaining profiles at the NAST-I FOVs, we then kept only those FOVs within 100 km and 1 h of the launches, which eliminated a small fraction of the FOVs (≃12.6%).

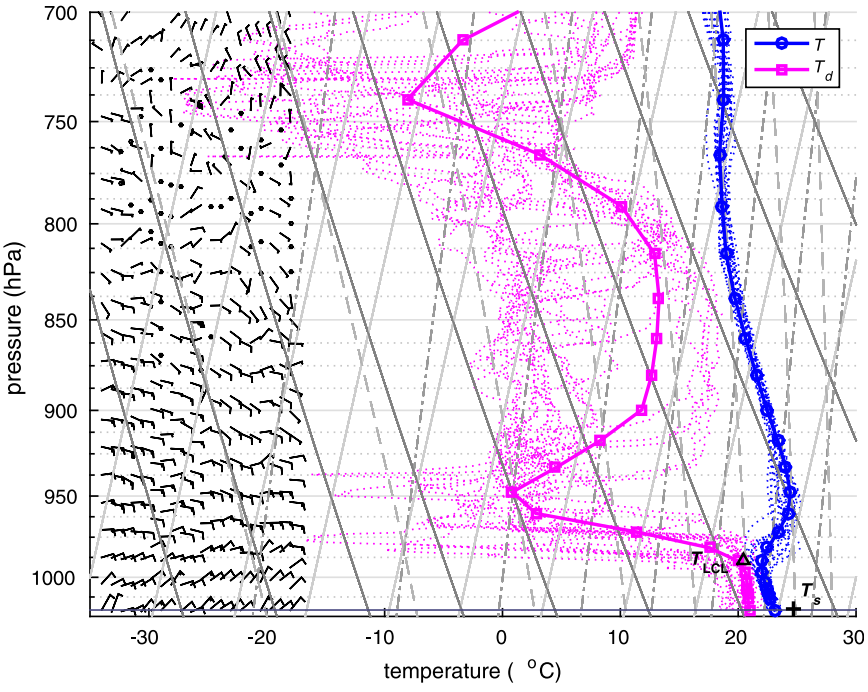

FIG. 5. Skew-T diagram showing dropsonde soundings deployed from the BAe 146 aircraft during JAIVEx (dotted lines, 20 total), along with the mean merged profiles for cloudy NAST-I FOVs (based on GOES AOD) at the reduced levels used for LBLRTM calculations (solid lines). The altitude and temperature of the mean LCL estimated from Eqs. (11) and (12) are shown with a black triangle, and the mean satellite-retrieved SST (RSS blended SST product) for the same FOVs is shown with a black +. Meteorological wind barbs for the 20 soundings are shown on the far left (in order of launch from left to right), with half and full feathers designating 2.5 and 5.0 m s^{-1}, respectively.

These space–time cutoffs were settled upon as a trade-off between minimizing mismatch error while retaining a large-enough sample (e.g., Sun et al. 2010), with flexibility granted to the spatial requirement as a result of using the ECMWF fields. Only one FOV fell outside the 1-h time matchup window; thus, the reduction in the sample size was primarily the result of the 100-km space matchup criterion.

Because the measurements were obtained from an aircraft, the viewing geometry was affected by the pitch and roll of the aircraft. Taking the longitudinal and lateral axes of the aircraft to be x and y, respectively, and realizing that ϑ is measured around the x axis, the nadir view angle corrected for roll ϑ_x and pitch ϑ_y is given by (Nalli et al. 2008a)

$$\vartheta' = \arccos[\cos(\vartheta - \vartheta_x)\cos(\vartheta_y)]. \qquad (9)$$

The zenith angle corrected for roll/pitch θ' can then be obtained from Eq. (7) as before by substituting in ϑ' and the time-varying height of the WB-57 aircraft. During JAIVEx the differences $\vartheta' - \vartheta$ ranged from $-17.1°$ to $22.1°$ but distributed primarily about $\simeq +0.5°$, with a smaller secondary mode about $+15°$ because of aircraft turnabouts.

Surface parameters were specified as follows. Surface wind speeds $\overline{u}$ at 10 m were necessary for SLR calculation as prescribed by Eq. (6); we used ECMWF surface wind fields (1200 UTC forecasts for 1500 and 2100 UTC, along with the 1800 analysis) linearly interpolated in space and time to the NAST-I FOV coordinates $\overline{u}(x, y, t)$. However, for skin SSTs T_s because calc − obs in a microwindow channel is very sensitive to T_s, we decided to utilize two independent satellite SST EDR products. The first dataset was composed of hourly 6-km GOES SSTs (NOAA/NESDIS 2003) (1500–2000 UTC) gridded at $0.05° \times 0.05°$, where we perform a linear space–time interpolation to the NAST-I FOV coordinates $T_s(x, y, t)$. Note that SSTs from GOES were the only means available for independently estimating the temporal variation of the SST field during the NAST-I sampling period. The GOES SSTs are IR based and are therefore cloud masked, but not free of any unintended cloud influences. Their usage thus constitutes an analysis using cloud-masked data independent of the sensor (NAST-I) zenith view angle. Figure 6 shows the

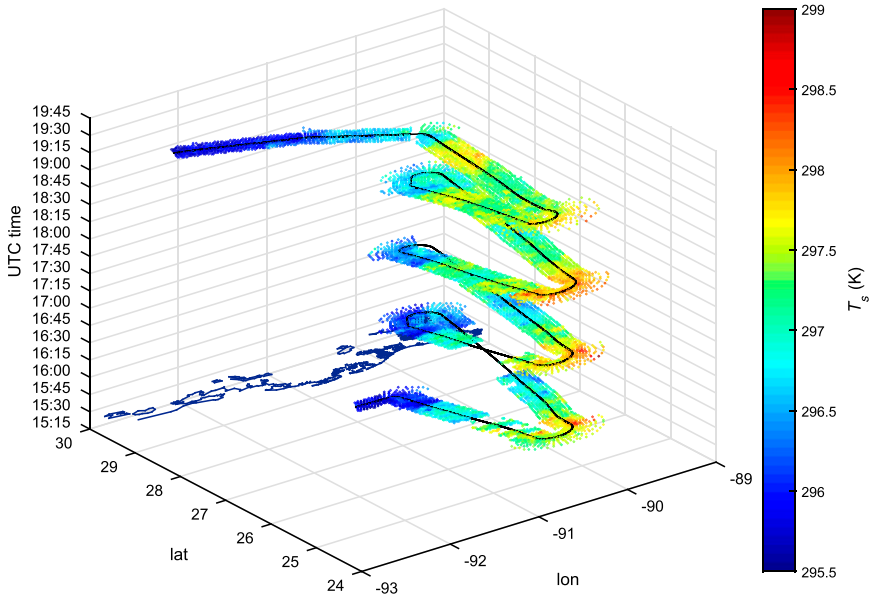

FIG. 6. As in Fig. 4, except showing GOES cloud-masked IR SST (6 km gridded at 0.05° × 0.05°, hourly 1500–2000 UTC).

space–time-interpolated GOES SSTs (analogous to the GASP AOD discussed above in Fig. 4) that were used in our analyses. Note that the regions where the GOES SST product was cloud masked (depicted as no data) correspond to the regions of heaviest FWC (depicted as large AOD $\gtrsim 0.25$ by GASP). Nevertheless, there remain regions where the FWC evaded cloud detection in the GOES SST product (potential implications of this are touched upon in section 3e). The second SST dataset was the Remote Sensing Systems, Inc. (RSS) Group for High Resolution Sea Surface Temperature (GHRSST) level 4 daily SST analysis (Remote Sensing Systems 2008) gridded at $\simeq 0.088° \times 0.088°$ using optimum interpolation (OI) of both MW and IR satellite measurements to allow for sampling under cloudy and elevated-aerosol conditions. The GHRSST product is expected to be minimally impacted by clouds or aerosols because the MW measurements serve as "anchor points," and thus, unlike the IR-based GOES SSTs, requires no cloud mask, providing T_s measurements for all the NAST-I FOVs. However, because it is limited to a daily temporal resolution, we can expect more overall random and systematic errors, the latter originating from diurnal T_s variations not captured in the daily composite.

d. Modeled LWIR impact of broken FWC clouds

To ascertain the angular impact of FWC clouds in the JAIVEx 29 April 2007 case on the clear-sky calc − obs described above, we utilize the sensitivity equation for broken opaque clouds derived by Nalli et al. (2012)—namely,

$$\delta T_{Bc}(\nu,\theta,\alpha_c,T_s,T_c) \approx [1-P(\theta,\alpha_c)]\frac{\left[\frac{\partial B_\nu}{\partial T}\right]_{\overline{T}_{sc}}}{\left[\frac{\partial B_\nu}{\partial T}\right]_{\overline{T}_B}}\delta T_{sc}, \quad (10)$$

where δT_{Bc} is the equivalent brightness temperature sensitivity due to clouds, $P(\theta, \alpha_c)$ is the PCLoS for a Poisson-distributed cloud field (Taylor and Ellingson 2008) with individual clouds having vertical aspect ratios $\alpha_c \equiv \delta z/\delta x$; $\delta T_{sc} \equiv T_s - T_c$ is the difference between the surface and cloud temperatures T_s and T_c, respectively; $\overline{T}_{sc}$ is the average of T_s and T_c; and $\overline{T}_B$ is the average of T_s and the measured channel brightness temperature $T_B(\nu)$. The brackets with the subscripted variable indicate the partial derivative is to be evaluated at that value. We obtain T_s from the satellite products described in section 3c. To estimate T_c, we use the merged dropsonde-ECMWF surface layer air temperatures $T(p_s, x, y, t)$ and dewpoints $T_d(p_s, x, y, t)$ to calculate the mean LCL over the cloudy areas (identified by GASP AOD described more below). We calculate the LCL temperature for each NAST-I FOV using Eq. (21) of Inman (1969):

$$\begin{aligned} T_{\rm lcl}(x,y,t) &\approx T_d(p_s,x,y,t) - [b_0 + b_1 T_d(p_s,x,y,t) \\ &\quad - b_2 T(p_s,x,y,t)][T(p_s,x,y,t) - T_d(p_s,x,y,t)], \end{aligned} \quad (11)$$

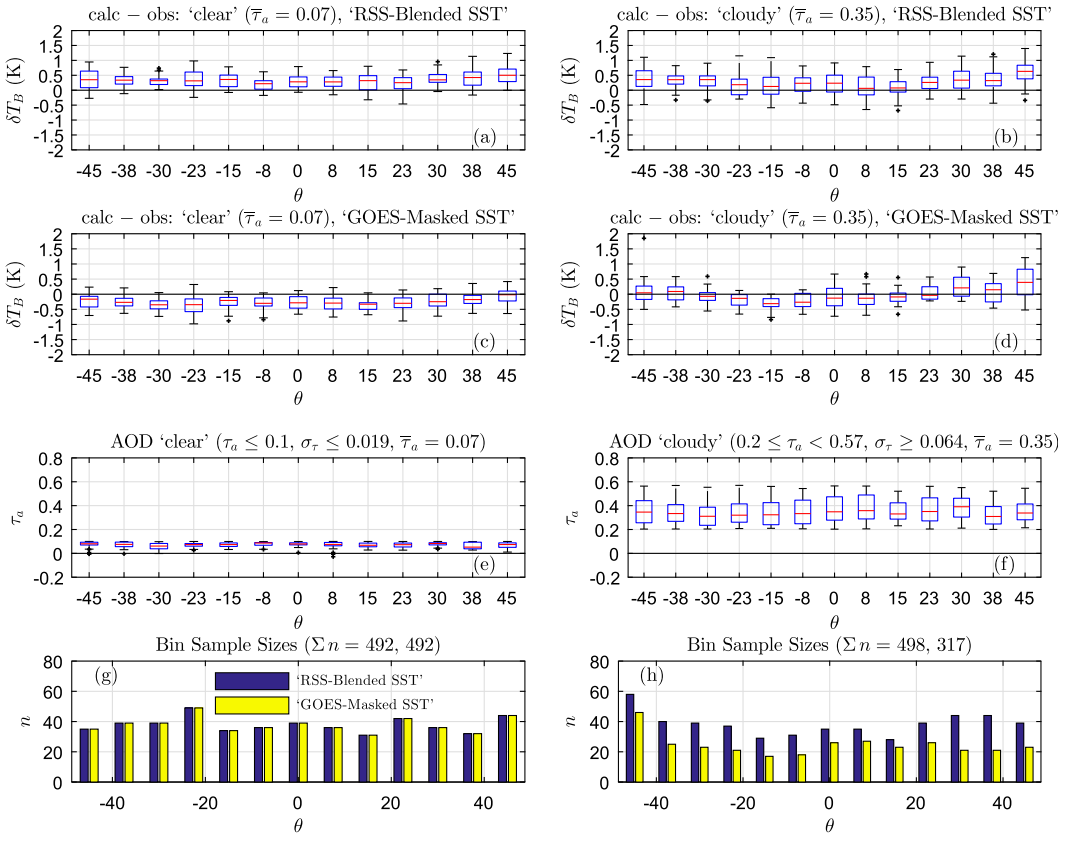

FIG. 7. Box-plot summary of calc − obs results as a function of zenith angle bin for the $\nu = [899.5, 901.8]\,\mathrm{cm}^{-1}$ microwindow; (left) clear and (right) cloudy bins: (a),(b) calc − obs using RSS blended GHRSST, (c),(d) calc − obs using GOES IR cloud-masked SST product, (e),(f) GOES AOD (GASP) for the two sky-condition bins, and (g),(h) angular bin sample sizes. Red lines and blue boxes depict medians and interquartile range, respectively; black "whiskers" depict remaining data spread excluding outliers, with black + signs designating the outliers.

where T and T_d are in units of kelvins or degrees Celsius, and the coefficients were evaluated to be $b_0 = 0.212$, $b_1 = 0.001\,571$, and $b_2 = 0.000\,436$. The LCL height is calculated using the Espy approximation (e.g., Lawrence 2005):

$$z_{\mathrm{lcl}}(x,y,t) \approx 125[T(p_s,x,y,t) - T_d(p_s,x,y,t)], \qquad (12)$$

where z_{lcl} is in meters, and the coefficient 125 is an approximate dry adiabatic lapse rate ($\mathrm{m\,K^{-1}}$ or $\mathrm{m\,°C^{-1}}$).

We can estimate the cloud-base height from Eq. (12), $z_c \approx z_{\mathrm{lcl}}$ (Stull 1988, p. 552), and the cloud temperature from Eq. (11), $T_c \approx T_{\mathrm{lcl}}$. However, to calculate $P(\theta, \alpha_c)$, it is necessary to obtain an estimate of the cloud aspect ratios α_c. We were not aware of a straightforward method of doing this using the thermodynamic data alone, so we sought an alternative approach—namely, to utilize the all-sky camera imagery (described in section 3a) for analyzing the shadows cast by the FWC observed during JAIVEx onto the sun-glint region. For complete details on our method for obtaining α_c from cloud shadow lengths, the reader is referred to appendix C. Using this approach, we estimated the cloud aspect ratios for semiellipsoidal cloud shapes to be $\alpha_c = 0.76$ and 1.04 for estimated cloud horizonal dimensions $\delta x = 0.3$ and 0.4 km, respectively (cf. appendix C). We note that our estimate of α_c implies FWC clouds with dimensions all being roughly the same—namely, cloud-base heights, horizontal diameters, and vertical extents $z_c \simeq \delta x \simeq \delta z \simeq 0.3$ km, respectively.

Because the dropsonde data show a stable capping inversion above a shallow mixed layer (Fig. 5), we would expect these FWC clouds to be "forced" (i.e., forced primarily by the original mixed-layer thermal) as opposed to "active" (i.e., cloud buoyancy beyond the thermal due to latent heat release) according to the cloud classification of Stull (1985). Translating to World Meteorological Organization (WMO) cloud definitions, forced clouds are typically cumulus humilis (i.e., slight vertical extent) but also possibly cumulus mediocris (i.e., moderate vertical extent) (WMO 1956, 1987; Stull 1985). However, the shadow analysis conducted in

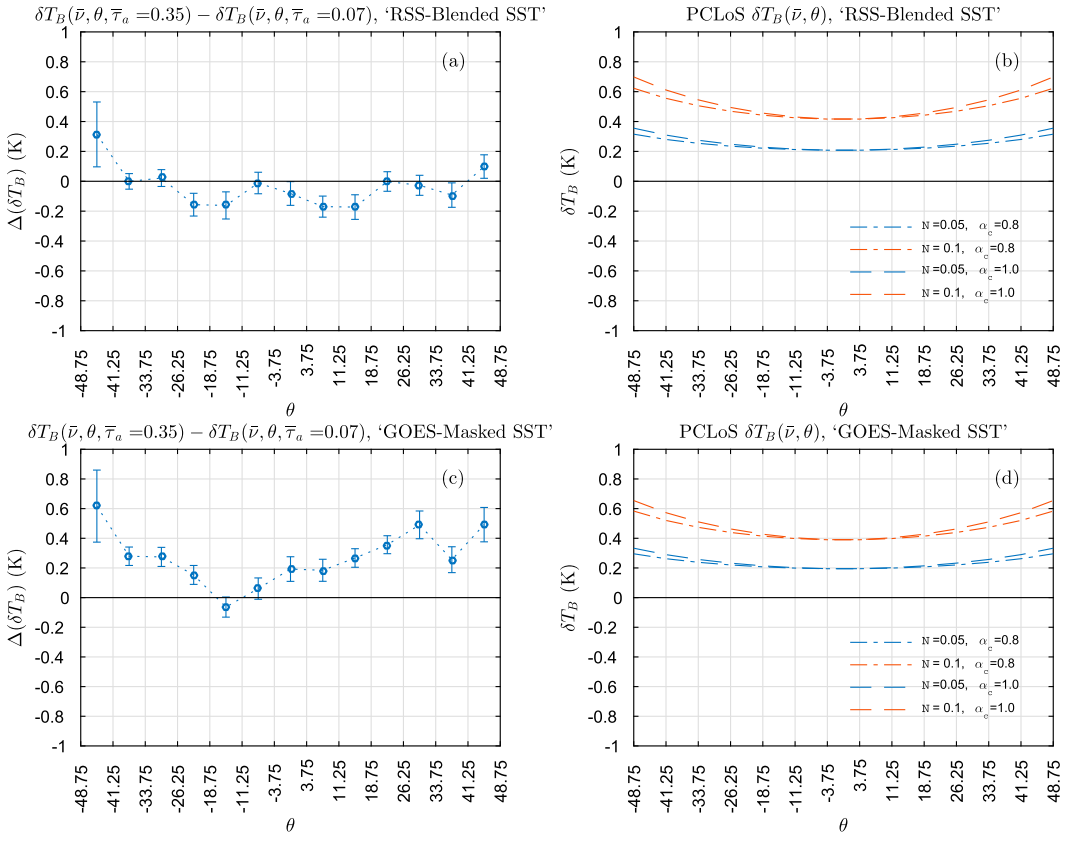

FIG. 8. (left) Double differences of mean calc − obs, for microwindow channel $\nu = [899.5, 901.8]$ cm^{-1}, in angular bins calculated from Eq. (13), with error bars denoting the standard errors of the differences σ_Δ calculated from Eq. (14) vs (right) modeled brightness temperature differences calculated from Eq. (10) for various combinations of cloud parameters discussed in the text. Plots use (top) RSS blended and (bottom) GOES IR cloud-masked SSTs.

appendix C suggests $\alpha_c \simeq 0.75$–1.0, which indicates vertical development. According to WMO classification, such clouds would be designated as $C_L = 2$ (cumulus of moderate or strong vertical extent) (WMO 1956, p. 38 and 40). One possibility is that the thermals possessed enough buoyancy to penetrate the capping inversion by $\simeq 0.3$ km owing to the advecting of a cooler air mass over warmer SSTs (see Figs. 5 and 6). Another factor was the presence of moderate winds ($\simeq$5–7 m s^{-1}) throughout the shallow mixed layer and a small amount of vertical wind shear (as seen in Fig. 5) that can contribute to vertical development in cumulus clouds.

e. Results and discussion

To examine the impact of the observed FWC clouds (and residual ambient aerosols) on the angular variation of calc − obs analyses, we placed data in angular bins centered on the NAST-I nadir scan angles $|\vartheta_0| =$ 0°, 7.5°, 15°, …, 45° with boundaries $|\vartheta_{\text{bound}}| \equiv 3.75°$, 11.25°, …, 48.75°. Because of the aircraft roll/pitch discussed earlier, the NAST-I zenith view angles θ typically exhibited a small degree of scatter about ϑ_0, but aircraft banking during turnabouts caused larger deviations ($\simeq 15°$) that resulted in a small, asymmetric number of FOVs falling outside of the −45° and +45° bins (25 and 328, respectively). We further binned the data according to two sky conditions: ''clear'' and ''cloudy.'' To achieve this binning, we relied on the GASP data (AOD τ_a and AOD standard deviation σ_τ) as discussed in section 3b. NAST-I FOVs are binned as clear for $\tau_a \leq \mathscr{P}(\tau_a, 25) \wedge \sigma_\tau \leq \mathscr{P}(\sigma_\tau, 20)$, where $\mathscr{P}$ indicates percentile. Likewise, FOVs are binned as cloudy for $\mathscr{P}(\tau_a, 75) \leq \tau_a < \mathscr{P}(\tau_a, 99) \wedge \sigma_\tau \geq \mathscr{P}(\sigma_\tau, 95)$. These thresholds ensured ''pure'' binning given the uncertainties inherent in our FOV interpolation scheme (FOV remapping described in appendix B and especially the linear interpolation in time from 30-min GOES sampling to boundary layer time scales $\lesssim 10$ min), while retaining large enough sample sizes.

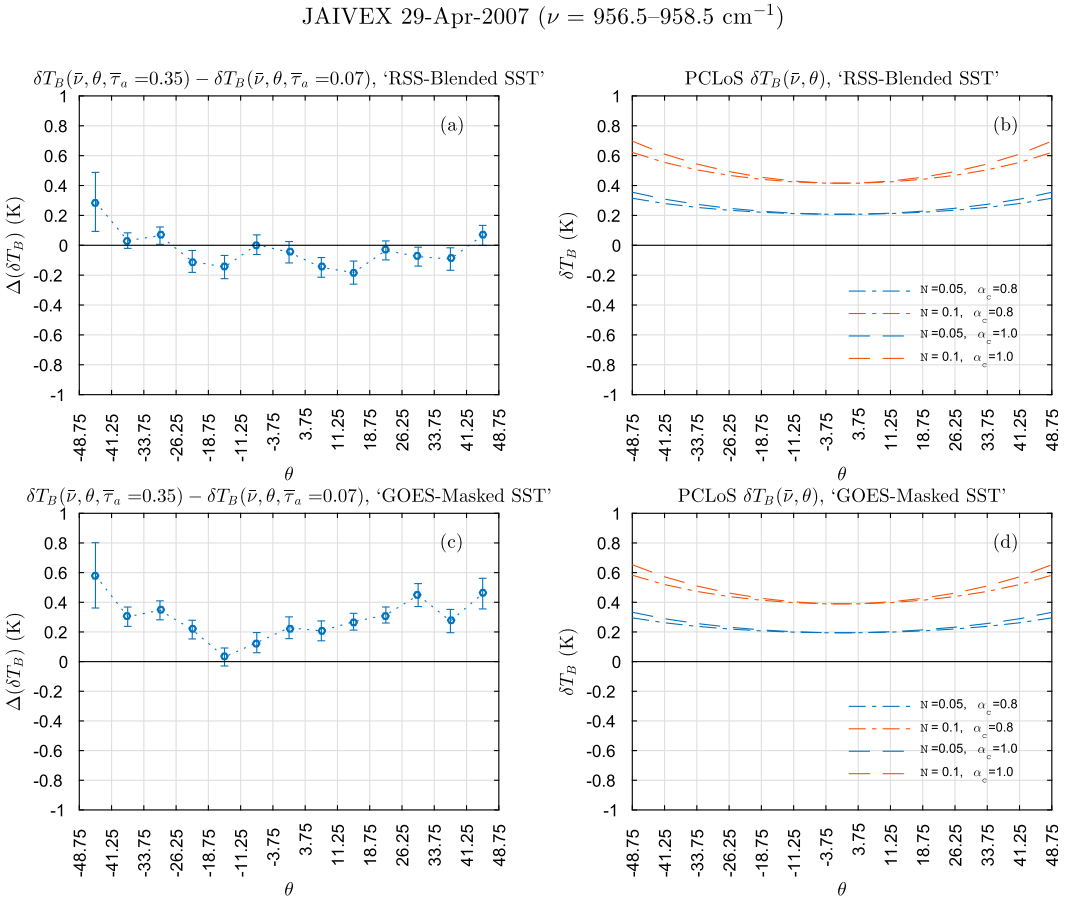

FIG. 9. As in Fig. 8, but for microwindow channel $\nu = [956.5, 958.5]\,\mathrm{cm}^{-1}$.

Figure 7 provides box plot statistical summaries of calc − obs results for the $\nu = [899.5, 901.8]\,\mathrm{cm}^{-1}$ microwindow; we note that the use of box plots provides robust statistical metrics that are insensitive to outliers without making any assumptions about the sample distributions. From the two bottom rows it can be seen that the sampling is reasonably uniform among the angular bins, in terms of AOD (i.e., sky conditions; Figs. 7e,f) and sample sizes (Figs. 7g,h). The GOES SST sample is reduced in the cloudy bin because of the cloud mask (Fig. 7h) as would be expected. In the top two rows one can see an increased concave-up calc − obs signal in the cloudy bin plots (right) versus the clear bin plots (left), with the RSS blended and GOES SSTs resulting in overall positive bias and negative bias, respectively. We do not know exactly why the two SST datasets result in these differing biases, but it is plausible that there could be bias in the RSS blended data owing to diurnal variations not resolved by the daily compositing. It is less clear where the negative bias originates in the GOES SST, but it is conceivable that the IR-based GOES SST product would suffer from residual cloud contamination in FOVs eluding the cloud mask (a primary thesis of this paper).

To examine more closely the impact of clouds (and/or aerosols) on these results, we computed angular bin calc − obs "double differences" between the clear and cloudy bins for the microwindow channels discussed in section 2a. We derive the mean double difference for angular bins $\delta\theta$ as

$$\Delta[\delta T_B(\overline{\nu},\delta\theta)] = \langle[\hat{T}_B(\overline{\nu},\theta) - T_B(\overline{\nu},\theta)]_{\mathrm{cld}}\rangle_{\delta\theta} - \langle[\hat{T}_B(\overline{\nu},\theta) - T_B(\overline{\nu},\theta)]_{\mathrm{clr}}\rangle_{\delta\theta}, \quad (13)$$

where angle brackets denote averages of the angular bin $\delta\theta$ and "cld" and "clr" denote FOVs for the cloudy and clear bins. Assuming statistical independence between the cloudy and clear averages, we may calculate the standard error of the double differences as (Mandel 1984, p. 110)

$$\sigma_\Delta(\delta\theta) = \sqrt{\frac{\sigma^2_{\mathrm{cld}}(\delta\theta)}{n_{\mathrm{cld}}(\delta\theta)} + \frac{\sigma^2_{\mathrm{clr}}(\delta\theta)}{n_{\mathrm{clr}}(\delta\theta)}}, \quad (14)$$

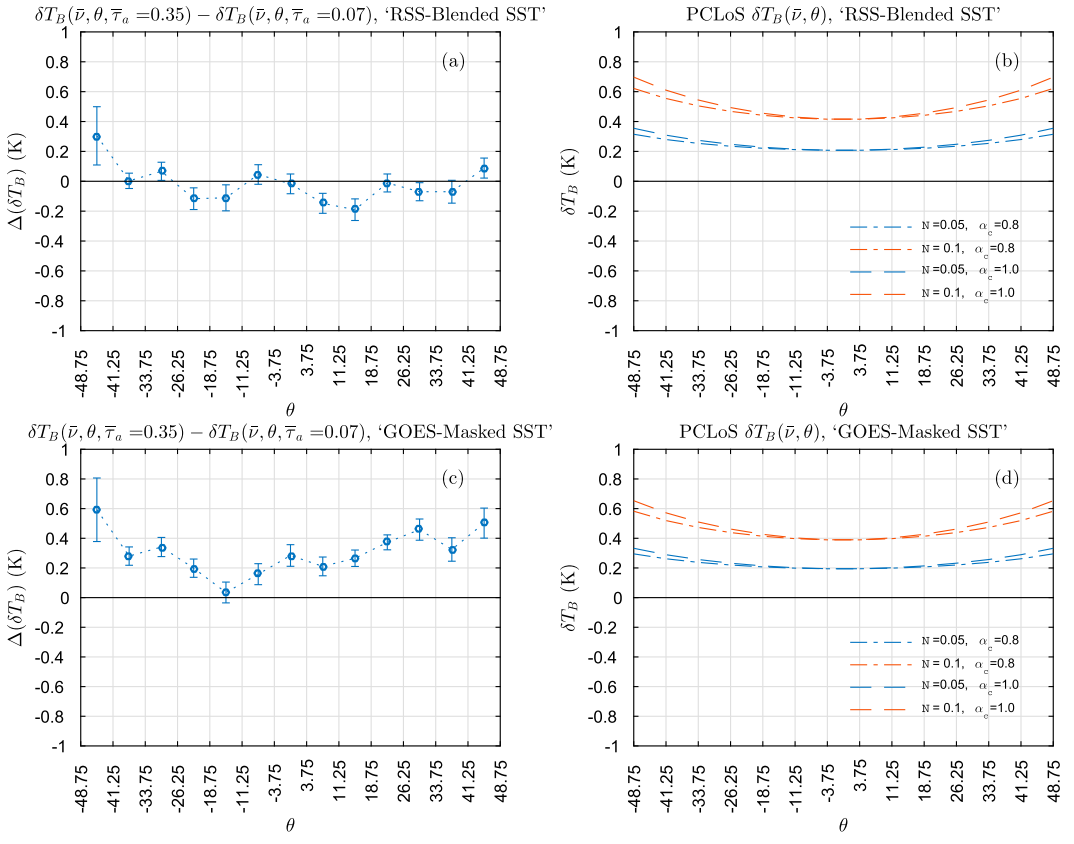

FIG. 10. As in Fig. 8, but for microwindow channel $\nu = [962.5, 964.5]$ cm^{-1}.

where σ^2 and n denote the variances and sample sizes in the cloudy (cld) and clear (clr) angular bins $\delta\theta$. The double-difference results for the microwindow channels defined in section 2a are shown in left columns of Figs. 8–10, with the PCLoS predicted brightness temperature differences (described in section 3d) computed from the PCLoS sensitivity Eq. (10) shown in the right plots. The PCLoS modeled results are derived for four combinations of cloud parameters—namely, aspect ratios $\alpha_c = \{0.8, 1.0\}$ and assumed cloud fractions $N = \{0.05, 0.1\}$. The choice of aspect ratios are based upon our analysis of the cloud shadows as discussed in appendix C. Using Eq. (11), we determined the mean LCL temperature for the cloudy bin to be $\overline{T}_{\rm lcl} \simeq 293.6$ K; the corresponding mean RSS and GOES SSTs were $\overline{T}_s \simeq 297.8$ and 297.5 K, respectively.

Calculations using the GOES IR SST (Figs. 8c, 9c, and 10c) are more consistent with the modeled results (Figs. 8d, 9d, and 10d), especially in the sense that there is a positive bias throughout the scan as would be expected. It is not clear why the results using RSS blended SSTs show near-zero bias (even slightly negative) at the smaller angles, although it may be related to unresolved spatiotemporal features in the dataset. It can be seen that results for these microwindows are very similar to one another, thus providing us greater confidence in our calculations.[3] Regardless of the SST dataset, there are distinct concave-up signals in the double-difference plots (Figs. 8a,c, 9a,c, and 10a,c) ranging from ≃0.2 to 0.4 K. These are consistent in magnitude (albeit somewhat larger) with the δT_B predicted by Eq. (10)—that is, ≃0.1–0.2 K. Based on the estimated $\overline{T}_s$ and $\overline{T}_{\rm lcl}$, the results from Eq. (10) suggest an average absolute cloud fraction (in the cloudy bin) of $N \lesssim 0.05$ and aspect ratio $\alpha_c \gtrsim 1.0$.

We note these results are based upon a total of $N = 492$ clear and $N = 498$ (317 using GOES cloud-masked SST) cloudy observations located over broken FWC cloud

[3] We also performed calculations for additional LWIR microwindows, namely $\nu = [831.5, 834.0]$, [860.2, 864.0], and [933.4, 934.4] cm^{-1}, which yielded very similar results and thus are omitted in the interest of brevity.

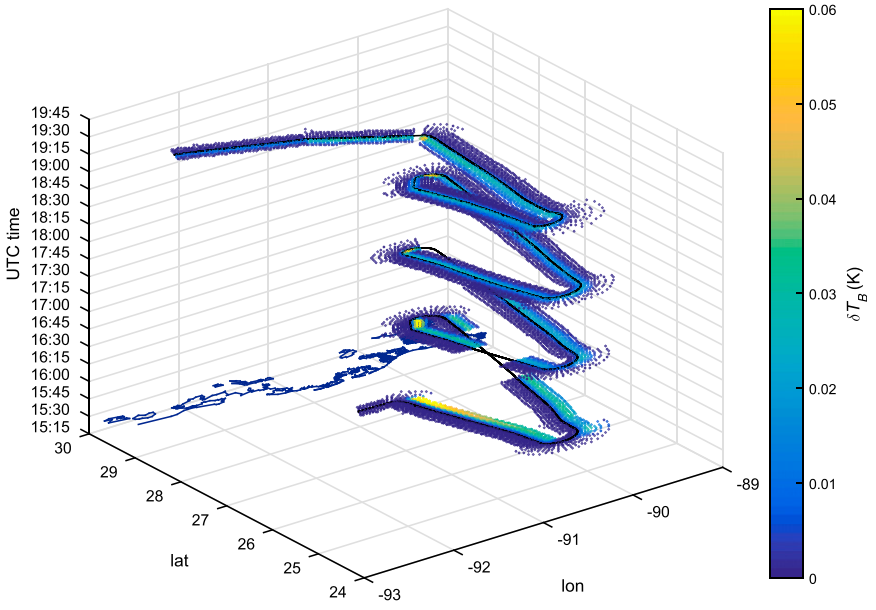

FIG. 11. As in Fig. 4, except showing the systematic impact of sun glint expressed as equivalent brightness temperatures for an LWIR microwindow channel ($\nu = 963.5\,\mathrm{cm}^{-1}$).

fields that are undoubtedly difficult to detect. Given our exploitation of hyperspectral microwindows that avoid gas absorption lines, sensitivity of the result to any random errors in the clear-column atmospheric state specification is considered small (assuming there is no systematic measurement error) and minimized by the double-differencing approach. We found calc − obs bias over MBL FWC cloud fields observed during the 29 April 2007 JAIVEx flight, whereby the overall cloud fractions were relatively small and the cloud temperatures were estimated to be only $\simeq$4 K cooler than the SST, are consistent with the theoretical sensitivity given by Eq. (10). Our experimental analysis of aircraft-based IR spectral data taken under these conditions thus corroborate previous sensitivity analyses (cf. Nalli et al. 2012), whereby such conditions can have a measurable concave-up impact on the angular agreement of calculations with observations. This supports the general hypothesis regarding the angular effect for ensembles of clear-sky window channel radiance observations contaminated by small amounts of undetected clouds and/or aerosols, assuming the occurrence of false negatives from cloud/aerosol detection algorithms under such conditions have negligible variation with view geometry.

In terms of EDR impact, assuming near-unity transmittance in surface-sensitive microwindow channels (e.g., the AIRS 2616 cm^{-1} "superwindow"), the angular variation of bias of surface skin/air temperature EDR retrievals from undetected clouds in clear-sky radiance products would be on the order of the inverse of those shown in Figs. 8–10 for calc − obs double differences (Figs. 8a,c, 9a,c, and 10a,c) and modeled PCLoS sensitivity (Figs. 8b,d, 9b,d, and 10b,d)—namely, from $\simeq -0.1$ to -0.4 K for $|\theta| \leq 45°$. As an additional note, in appendix A we also found the impact of sun glint in an LWIR microwindow ($\nu = 963.5\,\mathrm{cm}^{-1}$) reached magnitudes of $\simeq +0.06$ K in equivalent brightness temperatures (see Fig. 11), and this increases to $\simeq +0.15$ K for a microwindow located at 1203.25 cm^{-1}, which is otherwise a more transparent LWIR channel. Therefore, future aircraft-based satellite cal/val campaigns (conducted under clear-sky daytime conditions), especially those focused on high-accuracy SDR cal/val involving forward calculations (e.g., Newman et al. 2012; Nalli et al. 2013b), may consider accounting for sun glint in LWIR channels as outlined in this paper, as the glint effect can introduce angularly systematic radiance contributions close to the same order of magnitude as the observed microscale cloud effect.

Finally, it is also worth noting that our papers on the angular effect of clouds have methodically extended the application of the PCLoS model, including three general cloud shapes, from visual-based remote sensing and radiative flux applications (e.g., Taylor and Ellingson 2008) to passive IR remote sensing applications. In this paper we have extended our applications of the PCLoS model toward the estimation of cloud aspect ratios from cloud shadows, which we envision may be useful for future aircraft campaigns equipped with all-sky cameras, or in analyses of clouds within satellite visible

imagery, or in future applications where cloud shadowing might be of interest (e.g., radiative transfer in atmospheres with one than more cloud layer).

Acknowledgments. This research was supported by the NOAA Joint Polar Satellite System (JPSS-STAR) Office (L. Zhou) and the NOAA/NESDIS/STAR Satellite Meteorology and Climatology Division (SMCD) (F. Weng). We are grateful to the following individuals for their contributions in support of this work: V. Leslie (MIT Lincoln Lab) for providing the all-sky camera images and for discussions pertaining to the image timestamp offset, S. Kondragunta and C. Xu (NESDIS/STAR) for providing the NOAA GASP aerosol EDR product for April 2007, A. Ignatov and X. Liang (NESDIS/STAR) for bringing our attention to the possibility of sun-glint contamination in LWIR channels, and C. D. Barnet (STC, formerly NESDIS/STAR) for his support of the earlier related papers. We also thank the three anonymous reviewers who carefully reviewed two manuscript iterations and provided constructive feedback that we used to strengthen the quality of the final paper. Determination of the local solar zenith and azimuth angles for the JAIVEx glint analysis was made possible via code developed by V. Roy and distributed at the MATLAB Central File Exchange (sun_position.m). The views, opinions, and findings contained in this paper are those of the authors and should not be construed as an official NOAA or U.S. Government position, policy, or decision.

APPENDIX A

Sun-Glint Calculation

As discussed above in section 2c, sun glint is an issue in the JAIVEx dataset that must be taken into consideration. It is clearly evident in the hemispheric camera images (e.g., Fig. 2) that the reflected solar disk systematically persists near nadir throughout the observing period. Because the aircraft flight path assumed a predominately north–south course, angular scanning was predominately east–west over a continuous limited space–time domain. This means that, unlike the satellite-based analyses in Nalli et al. (2013a), the magnitude of LWIR sun glint in the JAIVEx NAST-I data will have a systematic angular dependence. We accounted for this problem by calculating the reflected solar radiance as described below.

Under the assumption of negligible scattering in the IR, we can ignore reflected diffuse solar contributions outside the solid angle subtended by the solar disk $\delta\Omega_\odot$, such that $r_\nu(\theta', \theta; \phi', \phi) I^{\downarrow}_{\nu\odot}(p_s, \theta', \phi') = 0$ for $\theta' \approx \theta_\odot \vee \phi' \approx \phi_\odot$, thus behaving as $r_\nu(\theta', \theta; \phi', \phi)\delta(\theta' - \theta_\odot)\delta(\phi' - \phi_\odot) I^{\downarrow}_{\nu\odot}(p_s, \theta', \phi')$ [e.g., Thomas and Stamnes (1999), p. 171]. The solar component of the double-integral term in Eq. (2) may then be simplified

$$\int_0^{2\pi}\int_0^{\pi/2} r_\nu(\theta', \theta; \phi', \phi)\delta(\theta' - \theta_\odot)\delta(\phi' - \phi_\odot) I^{\downarrow}_{\nu\odot}(p_s, \theta', \phi') \cos(\theta') \sin(\theta')\, d\theta'\, d\phi'$$
$$= r_\nu(\theta_\odot, \theta; \phi_\odot, \phi) \int_0^{2\pi}\int_0^{\pi/2} I^{\downarrow}_{\nu\odot}(p_s, \theta', \phi') \cos(\theta') \sin(\theta')\, d\theta'\, d\phi' = r_\nu(\theta_\odot, \theta; \phi_\odot, \phi) L^{\downarrow}_{\nu\odot}(p_s, \theta_\odot), \tag{A1}$$

where $L^{\downarrow}_{\nu\odot}(p_s, \theta_\odot)$ is the solar luminosity at the surface defined as (Goody and Yung 1989; Merchant et al. 2009)

$$L^{\downarrow}_{\nu\odot}(p_s, \theta_\odot) = [\bar{I}_{\nu\odot}(0)\delta\Omega_\odot]\mathscr{T}_\nu(0, \theta_\odot), \tag{A2}$$

with a mean intensity of the solar disk subtending solid angle $\delta\Omega_\odot$ at the TOA defined as (Goody and Yung 1989, p. 18)

$$\bar{I}_{\nu\odot}(0) \equiv \frac{\int_{\delta\Omega_\odot} \cos(\theta_\odot) I^{\downarrow}_{\nu\odot}(0, \Omega')\, d\Omega'}{\int_{\delta\Omega_\odot} \cos(\theta_\odot)\, d\Omega'}. \tag{A3}$$

The bracketed term in Eq. (A2) $\bar{I}_{\nu\odot}(0)\delta\Omega_\odot$ is the solar irradiance (Goody and Yung 1989, p. 18), and the mean solar intensity can be calculated treating the sun as a blackbody emitting at effective emission temperature $T_\odot$—that is, $\bar{I}_{\nu\odot}(0) = B_\nu(T_\odot)$. Goody and Yung (1989) give effective emission temperatures for 5 and 10 μm as 5500 and 5050 K, respectively; thus, for LWIR calculations we use $T_\odot = 5050$ K.

In calculating the sun-glint bidirectional reflectance term in Eq. (A1), it is first noted that the ocean surface behaves as a quasi-specular reflector (which commonly manifests itself in the solar spectrum as sun glint). Because the radii of curvature of the smallest capillary waves is much larger than the wavelength of radiation, the surface reflection may calculated assuming the geometrical optics limit (e.g., Cox 1974, 60–61), whereby individual wave facets are treated as a specular reflecting planes, which leads to quasi-specular reflection from

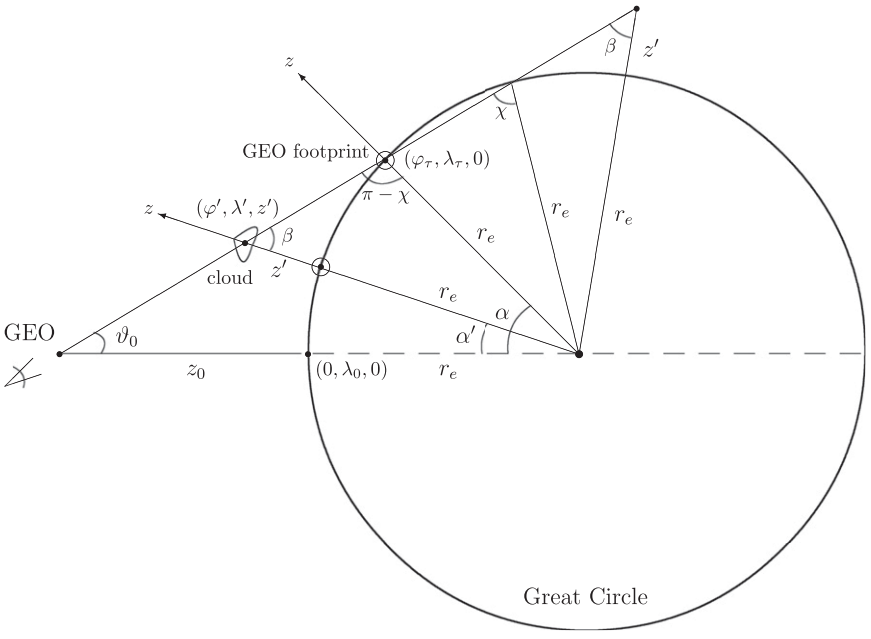

FIG. B1. Cross section (not drawn to scale) of a spherical Earth formed by the plane of the great circle traced along the line of sight of a GEO observer located at altitude z_0 and viewing at nadir view angle ϑ_0. The observed cloud (or aerosol layer) at (φ', λ', z') is reported at a surface footprint geolocated at $(\varphi_\tau, \lambda_\tau, 0)$, these forming great circle "longitude" angles from the subsatellite point $(0, \lambda_0, 0)$ of α' and α, respectively, both of which can be derived from plane geometry.

the entire surface. Given a wave-slope probability density function (PDF) $P_w(\sigma^2, \theta_n)$ describing a wave-slope distribution with facet zenith normal angles θ_n and variance σ^2, the solar bidirectional reflectance r_ν may be modeled as the contribution of specularly reflected rays given by (Bréon and Henriot 2006; Kay et al. 2009; Merchant et al. 2009; Zhang and Wang 2010; Jackson and Alpers 2010)

$$r_\nu(\theta_\odot, \theta; \phi_\odot, \phi) \approx \rho(N_\nu, \Theta_i) \frac{P_w(\sigma^2, \theta_n)}{4\cos(\theta)\cos^4(\theta_n)}, \tag{A4}$$

where Θ_i is the incidence angle of specularly oriented wave facets, θ_n is the facet normal zenith angle (frequently referred to as β in the literature), and ρ is the unpolarized Fresnel reflectance coefficient for radiance, all given by

$$\Theta_i = \frac{1}{2}\arccos[\cos(\theta_\odot)\cos(\theta) - \sin(\theta_\odot)\sin(\theta)\cos(\phi - \phi_\odot)], \tag{A5}$$

$$\theta_n = \arccos\left[\frac{\cos(\theta) + \cos(\theta_\odot)}{2\cos(\Theta_i)}\right], \tag{A6}$$

$$P_w(\sigma^2, \theta_n) = \frac{1}{2\pi\sigma^2}\exp\left[-\frac{1 - \cos^2(\theta_n)}{2\sigma^2\cos^2(\theta_n)}\right], \quad \text{and} \tag{A7}$$

$$\rho(N_\nu, \Theta_i) = \frac{1}{2}[|\rho_\parallel(N_\nu, \Theta_i)|^2 + |\rho_\perp(N_\nu, \Theta_i)|^2]; \tag{A8}$$

$\rho_\parallel$ and $\rho_\perp$ are the respective Fresnel amplitude reflectance coefficients corresponding to **E** fields parallel and perpendicular to the plane of incidence, and N_ν is the laboratory measured complex refractive index of seawater. For simplicity, in this work we utilize the Cox and Munk (1955) isotropic (as opposed to anisotropic) Gaussian PDF given by Eq. (A7), with mean square slopes modeled as a function the local mean surface wind speed $\overline{u}$; that is, $2\sigma^2 = 0.003 + 0.005\,12\overline{u}(z_s)$, where $z_s \equiv 12.5$ m. However, because surface wind speeds are conventionally reported at 10 m (including the ECMWF surface winds used in this paper), we also make use of the wind speed adjustment methodology described in Nalli et al. (2008b) (their appendix B) to convert the measured $\overline{u}$ at 10 m to the sea surface equivalent speed at 12.5 m.

Figure 11 shows the sun-glint equivalent brightness temperature differences for an LWIR microwindow

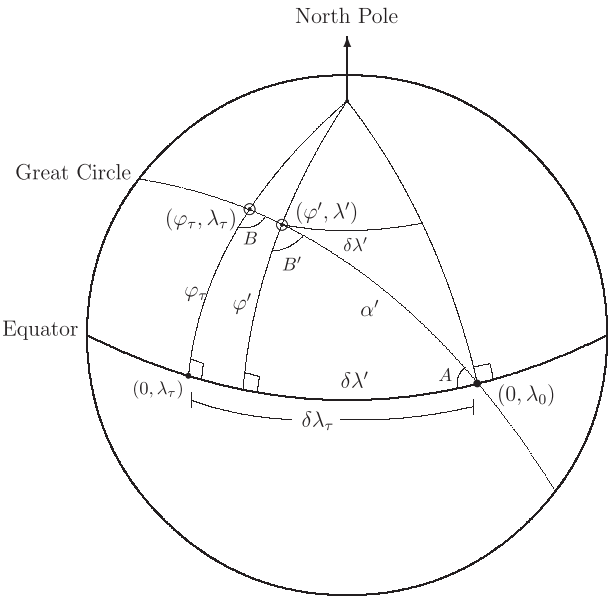

FIG. B2. Spherical geometry corresponding to the 2D cross section shown in Fig. B1. The great circle is shown under an arbitrary line of sight of a GEO observer located above the subsatellite point $(0, \lambda_0)$. The observed cloud (or aerosol layer) overlies (φ', λ') and is reported at a surface footprint geolocated at $(\varphi_\tau, \lambda_\tau)$. Longitudinal arcs $\delta\lambda_\tau$ and $\delta\lambda'$ are the relative longitudes with respect to the satellite at λ_0.

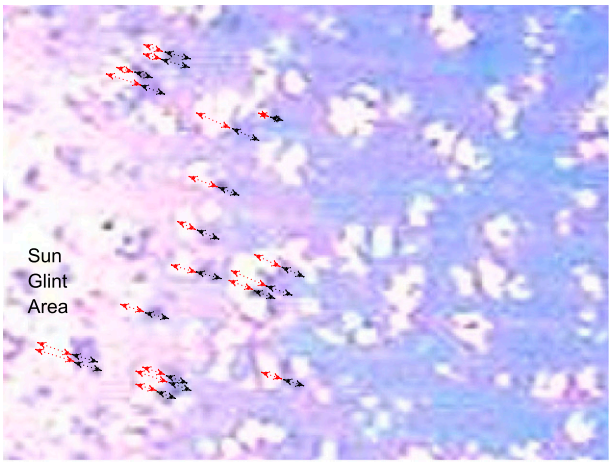

FIG. C1. Zoom of hemispheric camera image shown in center plot of Fig. 2 (1542:35 UTC 29 Apr 2007) showing comparative lengths of cloud horizontal extent (red) and the cloud shadows cast onto the edge of the sun-glint disk (black) for estimation of the cloud vertical aspect ratios α_c. Clouds with shadows are selected as close to the center of the image (nadir view) as possible (cf. Fig. 2). The cloud shadows visible to the camera (i.e., not hidden by the cloud) are seen to be roughly in the range of 0.5–1.0 times the diameter of the clouds δx, with smaller clouds casting relatively longer visible shadows.

$(\nu = 963.5\,\mathrm{cm}^{-1})$ at NAST-I FOVs throughout the JAIVEx 29 April 2007 flight calculated from

$$\delta T_B(\nu) = \delta I_{\nu\odot}(p_s, \theta_\odot)\left[\frac{\partial B_\nu}{\partial T}\right]^{-1}_{T_0}, \qquad \text{(A9)}$$

where $\delta I_{\nu\odot}(p_s, \theta_\odot) \equiv r_\nu(\theta_\odot, \theta; \phi_\odot, \phi) L^{\downarrow}_{\nu\odot}(p_s, \theta_\odot)$ and $T_0 = B_\nu^{-1}[R_\nu(p_0, \theta)]$. It can be seen that, in agreement with Závody and Birks (2004), the impact of sun glint in this LWIR microwindow, while small, nevertheless in this case reached as much as $\simeq +0.06$ K (this magnitude increases to $\simeq +0.15$ K at 1203.25 cm^{-1}; not shown).

APPENDIX B

Mapping GEO Cloud/Aerosol Layer Data to Aircraft Sensor Footprints

The aerosol or cloud signal observed within the FOVs of an aircraft sensor (e.g., NAST-I) geolocated to the surface "footprint" $(\varphi, \lambda, z = 0)$, where φ and λ are the latitude and longitude coordinates, respectively, corresponds to a cloud (or aerosol layer) located within the FOVs but at effective-layer altitude $z' > 0$ over a point (φ', λ', z') displaced from $(\varphi, \lambda, 0)$. This cloud (or aerosol layer) at (φ', λ', z') is seen within the FOVs of the GEO sensor (e.g., GOES Imager) geolocated to the surface footprint $(\varphi_\tau, \lambda_\tau, 0)$. Our task then was to perform the remapping $(\varphi, \lambda, 0) \rightarrow (\varphi', \lambda', z') \rightarrow (\varphi_\tau, \lambda_\tau, 0)$, given an estimate of z', after which the interpolation may be performed to obtain the AOD for the NAST-I FOVs as indicated in section 3b.

We first performed the mapping from $(\varphi, \lambda, 0) \rightarrow (\varphi', \lambda', z')$ by assuming the observer is of low-enough altitude to disregard Earth curvature and then proceeded to employ simple linear one-dimensional interpolations of coordinates (φ, λ, z) along the lines of sight in from the aircraft observer (NAST-I) at $(\varphi_{\mathrm{ac}}, \lambda_{\mathrm{ac}}, z_{\mathrm{ac}})$ to the surface footprints $(\varphi, \lambda, 0)$, with the cloud/aerosol location interpolated at (φ', λ', z') given $z_{\mathrm{ac}} > z' > 0$.

We then performed the remapping $(\varphi', \lambda', z') \rightarrow (\varphi_\tau, \lambda_\tau, 0)$ as follows. Figure B1 shows a cross section of Earth formed by the plane of the great circle traced by the line of sight of a GEO observer. The GEO observer is located at altitude z_0 and viewing at nadir view angle ϑ_0. The observed cloud (or aerosol) layer at (φ', λ', z') is reported at a surface footprint geolocated at $(\varphi_\tau, \lambda_\tau, 0)$, these forming great circle "longitude" angles from the subsatellite point $(0, \lambda_0, 0)$ of α' and α, respectively (these symbols not to be confused with cloud aspect ratio α_c). From the triangles formed by the GEO and Earth-center vertices with the cloud and GEO footprint vertices, the great circle angles α' and α are respectively given by

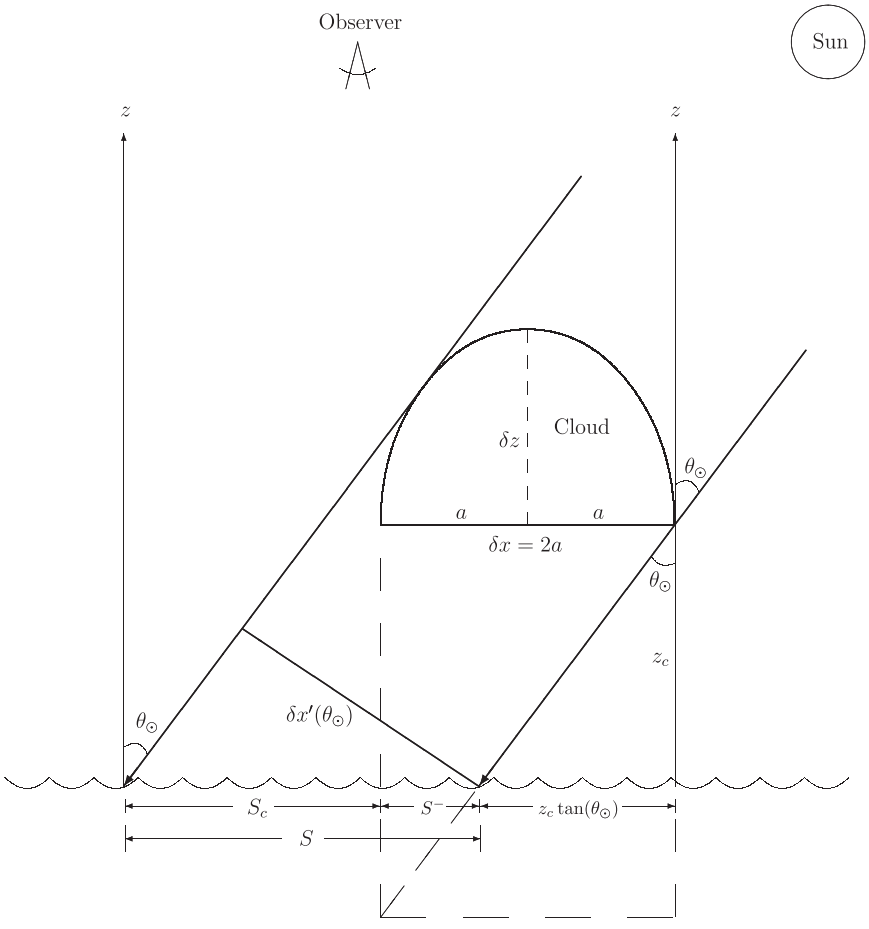

FIG. C2. Diagram showing geometry for deriving the cloud shadow cast onto the sun-glint region of Earth's surface and visible to an observer near zenith. An idealized hemispheroidal cloud shape is depicted as representative of FWC clouds (e.g., Nalli et al. 2012). The diagram shows the semiellipse cross section at the x–z plane, with the observer line of sight directed along the z axis and the solar azimuth along the x axis, and is drawn with the vertical semiminor axis $\delta z = 1.5a = 0.75\delta x$ ($\alpha = 0.75$). The sun and observer are taken to be far enough away such that rays are parallel, and the observer and cloud are taken to be on the edge of the sun-glint region, with the observer located near zenith and the cloud at an altitude low enough such that Earth curvature may be neglected.

$$\alpha' = \beta - \vartheta_0 \quad \text{and} \tag{B1}$$

$$\alpha = \chi - \vartheta_0, \tag{B2}$$

where angles β and χ are derived from the law of sines applied to the large triangles

$$\beta = \csc^{-1}\left[\frac{r_e + z'}{(r_e + z_0)\sin(\vartheta_0)}\right] \quad \text{and} \tag{B3}$$

$$\chi = \csc^{-1}\left[\frac{r_e}{(r_e + z_0)\sin(\vartheta_0)}\right]. \tag{B4}$$

To determine the displaced latitude–longitude (φ', λ'), we relied on spherical geometry as shown in Fig. B2. The great circle from Fig. B1 is shown under an arbitrary line of sight of the GEO observer located above the subsatellite point $(0, \lambda_0)$, where $\lambda_0 = -75°$ for *GOES-12*. The observed cloud (or aerosol layer) overlies (φ', λ') and is reported at a surface footprint geolocated at $(\varphi_\tau, \lambda_\tau)$. Given α', we determined the common angle A of the right spherical triangles as

$$A = \arccos[\tan(\delta\lambda')\cot(\alpha')], \tag{B5}$$

where $\delta\lambda'$ (and $\delta\lambda_\tau$) denote the relative longitudes (geocentric relative azimuth) defined as $\delta\lambda' \equiv \lambda_0 - \lambda'$ and $\delta\lambda_\tau \equiv \lambda_0 - \lambda_\tau$. From Eqs. (B1)–(B5), we finally obtained the corresponding GOES FOV latitude and longitude as

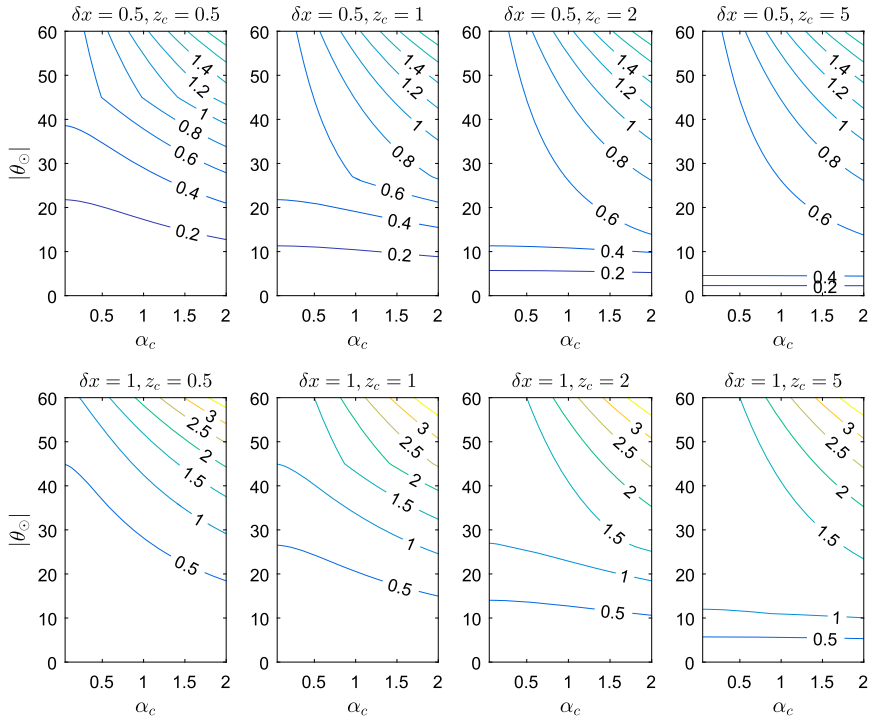

FIG. C3. Cloud shadow lengths S_c for assumed semiellipsoidal cloud shapes calculated from Eqs. (C2), (C3), and (C7), showing dependencies on parameters solar zenith angle $\theta_\odot$, cloud aspect ratio α_c, cloud horizontal dimension δx, and cloud-base height z_c.

$$\varphi_\tau = \arcsin[\sin(A)\sin(\alpha)] \quad \text{and} \tag{B6}$$

$$\lambda_\tau = \lambda_0 - \arcsin[\tan(\varphi_\tau)\cot(A)]. \tag{B7}$$

We then proceeded to obtain the values of AOD for the NAST-I FOVs via interpolation of the GOES AOD fields at $(\varphi_\tau, \lambda_\tau)$ as already discussed in in section 3b.

APPENDIX C

Estimating Cloud Aspect Ratios from Cloud Shadows

Figure C1 shows a zoom on an image of the broken FWC clouds observed during JAIVEx near the edge of the sun-glint region (the zoom is on the center image shown in Fig. 2), which is annotated to show estimates of the cloud horizontal dimensions versus the shadows they cast, these being visible over the sun-glint region. From geometric considerations discussed below, we consider only the shadows observed near the nadir angle of the observer (i.e., those near the center of the image), which are found near the edge of the sun-glint region owing to surface wave slopes oriented to reflect sun rays from the solar zenith angle to the observer. The observed cloud shadows are approximately in the range of 0.5–1.0 times the size of the cloud horizontal dimensions. We may then obtain the cloud aspect ratios α_c from the observed cloud shadows by modeling clouds as idealized cloud shapes as described below.

Here we restrict our consideration to the idealized cloud shapes considered previously by Nalli et al. (2012) based on the PCLoS cloud shape factors compiled by Taylor and Ellingson (2008), which include three basic forms—namely, isosceles trapezoids (including rectangles and triangles), spheroids (ellipsoids with equal horizontal semiaxes, $a = b$), and hemispheroids (semiellipsoids with $a = b$). We here note that these three idealized cloud shapes can model a large range of the basic morphologies assumed by real cloud forms. The hemispheroid (semiellipsoid) shape, possessing a rounded top and flat base, approximates cumulus clouds (Cu) with WMO classification $C_L =$ 1–3, or stratus (Sc) cloud type $C_L =$ 4 [e.g., WMO (1956), p. 40]. Isosceles trapezoids can model cumulonimbus cloud (Cb) types $C_L =$ 3, 9 (including anvil clouds) or cirrus (Ci) originating from Cb anvils, $C_H =$ 3 [e.g., WMO (1956), p. 40 and 53]. And finally, spheroids (ellipsoids) can otherwise approximate more nebulous Sc, Ci, and altocumulus (Ac) cloud forms lacking flat boundaries, $C_L =$ 4, 5, 8; $C_M =$ 3–5,

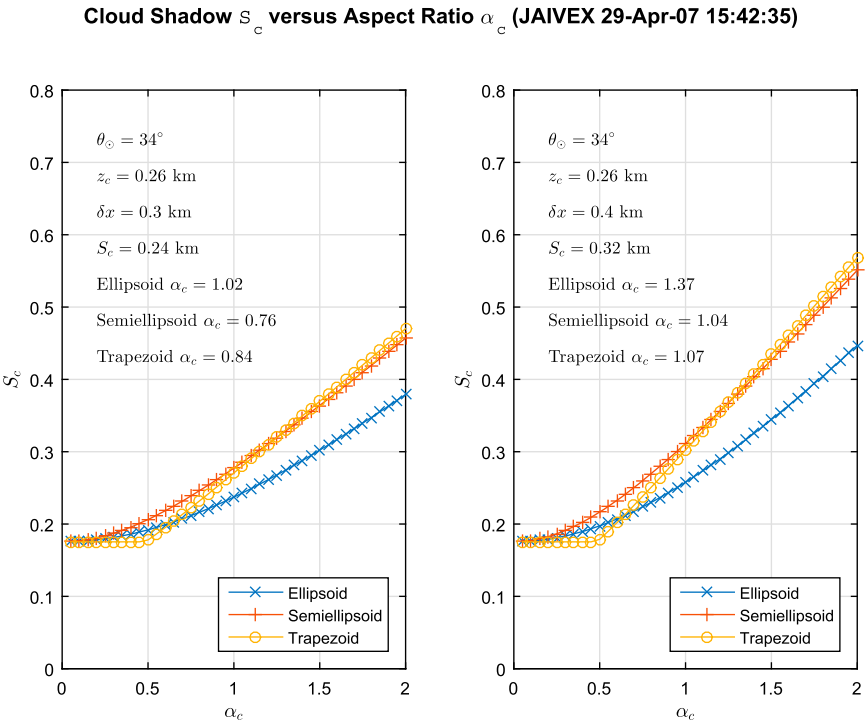

FIG. C4. Graphical illustration of the estimation of cloud aspect ratios for FWC clouds observed during the JAIVEx 29 Apr 2007 overflight. Plots show the variation of cloud shadow lengths S_c as a function of cloud aspect ratios α_c for clouds with estimated horizontal dimensions (left) $\delta x = 0.3$ and (right) 0.4 km. Given observed $S_c \simeq 0.8\delta x$ (cf. Fig. 14), one can visually find corresponding α_c for ellipsoid, semiellipsoid, and isosceles trapezoid ($\zeta_c = 33.75°$) cloud shapes by tracing the curves in the figures; the α_c values shown in the annotated text are the precise values calculated by finding the zeros of Eqs. (C2), (C3), and (C7).

7–9; or $C_H = 1, 2, 9$ [e.g., WMO (1956), p. 40, 47, and 53].

For simplicity, in the current work we assume clouds close enough to the surface to disregard Earth curvature (as would be the case for most opaque water-droplet clouds and certainly FWC); the observer is assumed to be near zenith, and both the sun and observer are considered far enough away such that rays may be assumed parallel. Figure C2 shows the two-dimensional (2D) geometry for an assumed hemispheroidal (semiellipsoidal) cloud shape, which also applies to the other idealized cloud shapes without loss of generality, hemispheroidal cloud shapes being considered good for representing FWC (as implied in the above paragraph). The figure specifically shows the semiellipsoidal cross section in the x–z plane with the solar azimuth oriented along the x axis. Given the geometrical optics limit valid for visible spectrum wavelengths, the width of a shadow cast by an opaque cloud is equivalent to the 2D cross section of the cloud perpendicular to the incoming solar rays; for a nonspherical cloud shape, the linear cross section will vary with the solar incidence angle. Nalli et al. (2012) derived equivalent expressions for calculating mean slant paths through semitransparent clouds that can be utilized for the present application—namely, $\delta x'(\theta) \equiv x'_2(\theta) - x'_1(\theta)$, where $x'_1(\theta)$ and $x'_2(\theta)$ are the limits of the cloud along an axis x' rotated by θ from x. For more on the geometry and derivations of $\delta x'(\theta)$ for various cloud shapes, the reader is referred to Nalli et al. (2012). In the present application, the rotation angle is equal to the solar zenith angle $\theta = \theta_\odot$.

The length of the cloud shadow projected onto Earth's surface is then given by

$$S(\theta_\odot) = \delta x'(\theta_\odot)\sec(\theta_\odot), \tag{C1}$$

and the portion of this shadow visible to an observer near the zenith is

$$S_c(\theta_\odot) = S(\theta_\odot) - S^-(\theta_\odot), \tag{C2}$$

where S^- is the portion the shadow S hidden from view by the cloud. We obtain the expression for S^- from the trigonometric relation for the right triangle under the cloud

$$S^{-}(\theta_{\odot}, z_c, \delta x) = \begin{cases} \delta x - z_c \tan(\theta_{\odot}), & |z_c \tan(\theta_{\odot})| < \delta x \\ 0, & |z_c \tan(\theta_{\odot})| \geq \delta x \end{cases}, \tag{C3}$$

where z_c is the cloud-base height and noting that $|z_c \tan(\theta_{\odot})| \geq \delta x$ implies the shadow is cast beyond the cloud such that none of it is obstructed from view (i.e., $S^{-} = 0$).

Using the expressions for $\delta x'(\theta_{\odot})$ from Nalli et al. (2012) for the three idealized cloud shapes, the 2D cloud shadow projected onto the surface [the first term in brackets on the right side of Eq. (C2)] S then takes the following forms. First, for trapezoidal cloud shapes with inclination angle of the cloud sides ζ_c (assuming square bases and edges aligned parallel with the sun's azimuth direction x), we have

$$S(\theta_{\odot}, \alpha_c, \zeta_c, \delta x) = \begin{cases} \delta x, & |\theta_{\odot}| < \zeta_c \\ \delta x \sec(\theta_{\odot}) \alpha_c \dfrac{\cos(\theta_{\odot} - \theta_d)}{\sin(\theta_d)}, & |\theta_{\odot}| \geq \zeta_c \end{cases}, \quad \text{isosceles trapezoid shadow}, \tag{C4}$$

where θ_d is the angle of the trapezoid diagonal given by

$$\theta_d = \arctan\left(\frac{\alpha_c}{1 - \alpha_c \tan\zeta_c}\right). \tag{C5}$$

Note that rectangular and triangular cloud shapes, being special cases of trapezoids, are simply given by inclination angles $\zeta_c = 0$ and $\zeta_c = \max(\zeta_c) = \arctan(1/2\alpha_c)$, respectively (Nalli et al. 2012). For ellipsoidal cloud shapes, we have

$$S(\theta_{\odot}, \alpha_c, \delta x) = \delta x \sec(\theta_{\odot}) \sqrt{(1 - \alpha_c^2)\cos^2(\theta_{\odot}) + \alpha^2}, \quad \text{ellipsoid shadow}, \tag{C6}$$

and for semiellipses

$$S(\theta_{\odot}, \alpha_c, \delta x) = \delta x \sec(\theta_{\odot}) \frac{1}{2}\left[\cos(\theta_{\odot}) + \sqrt{(1 - 4\alpha_c^2)\cos^2(\theta_{\odot}) + 4\alpha_c^2}\right], \quad \text{semiellipsoid shadow}. \tag{C7}$$

Thus, given Eq. (C3), along with either of Eq. (C4), (C6), or (C7), we can calculate the cloud shadow projected on Earth's surface visible to an observer near zenith, $S_c = S_c(\theta_{\odot}, \alpha_c, z_c, \delta x)$, from Eq. (C2), given the solar zenith angle $\theta_{\odot}$ and cloud aspect ratio α_c, base height z_c, and horizontal dimension δx. Figure C3 shows the calculated shadow lengths for semiellipsoid cloud shapes. Units for δx and z_c are arbitrary but consistent. Shadows increase primarily with increasing $\theta_{\odot}$ and δx, as would be expected. Similar patterns are observed for trapezoidal and ellipsoidal cloud shapes but are omitted in the interest of space constraints. Given these formulations, we can now solve Eq. (C2) for α_c by finding the zeros of the equation given S_c, $\theta_{\odot}$, z_c, and δx. From the all-sky images, specifically the sample image shown in Fig. C1, we can take the cloud shadows to be approximately $S_c \simeq 0.8\delta x$. We obtain a rough estimate of δx from considering a box centered on an all-sky image (e.g., the center image of Fig. 2) that is sufficiently small to be assumed flat; for simplicity, we select the box to span 10% of total image width. Taking the visible edge of the image to be a nadir angle of approximately |85°| (which corresponds to a zenith angle of $\simeq 87.26°$), the central box then corresponds to $\delta\theta \simeq \pm 8.5°$ (given the near-linear variation between linear distance and angle for small angles). The approximate expanse of the box δX is then given by the trigonometric expression $\delta X = 2z_{\mathrm{ac}}\tan(\delta\theta)$, where z_{ac} is the aircraft height ($\simeq$17 km), thus yielding $\delta X \approx 5.1$ km (figure not shown in the interest of page constraints). From this approximation, we were able to estimate the cloud diameters δx to be roughly on the order of 0.2–0.5 km, which are physically reasonable values for microscale FWC and consistent with the sounding data. Finally, given the mean cloud-base height as estimated from the LCL derived from the dropsonde data (during the time of the all-sky camera image) and Eq. (12), $z_c \simeq 0.26$ km (cf. Fig. 5), along with the solar zenith angle (derived from the UTC time and location) $\theta_{\odot} \simeq 34°$, we are able to estimate the cloud aspect ratios for semiellipsoidal clouds as $\alpha_c = 0.76$ and 1.04 for $\delta x = 0.3$ and 0.4 km, respectively, as illustrated in Fig. C4. Note that larger aspect ratios are derived from the other two cloud shapes.

REFERENCES

Arndt, D. S., M. O. Baringer, and M. R. Johnson, 2010: State of the Climate in 2009. *Bull. Amer. Meteor. Soc.*, **91**, s1–s222, doi:10.1175/BAMS-91-7-StateoftheClimate.

Benner, T. C., and J. A. Curry, 1998: Characteristics of small tropical cumulus clouds and their impact on the environment. *J. Geophys. Res.*, **103**, 28 753–28 767, doi:10.1029/98JD02579.

Bréon, F. M., and N. Henriot, 2006: Spaceborne observations of ocean glint reflection and modeling of wave slope distributions. *J. Geophys. Res.*, **111**, C06005, doi:10.1029/2005JC003343.

Cayla, F.-R., 1993: IASI infrared interferometer for operations and research. *High Spectral Resolution Infrared Remote Sensing for Earth's Weather and Climate Studies*, A. Chedin, M. T. Chahine, and N. A. Scott, Eds., NATO ASI Series, Vol. 19, Springer-Verlag, 9–19.

Chahine, M. T., and Coauthors, 2006: AIRS: Improving weather forecasting and providing new data on greenhouse gases. *Bull. Amer. Meteor. Soc.*, **87**, 911–926, doi:10.1175/BAMS-87-7-911.

Clough, S. A., M. W. Shephard, E. J. Mlawer, J. S. Delamere, M. J. Iacono, K. Cady-Pereira, S. Boukabara, and P. D. Brown, 2005: Atmospheric radiative transfer modeling: A summary of the AER codes. *J. Quant. Spectrosc. Radiat. Transfer*, **91**, 233–244, doi:10.1016/j.jqsrt.2004.05.058.

Cox, C., and W. Munk, 1955: Some problems in optical oceanography. *J. Mar. Res.*, **14**, 63–78.

——, 1974: Refraction and reflection of light at the sea surface. *Optical Aspects of Oceanography*, N. Jerlov and E. Nielsen, Eds., Academic Press, 51–75.

Goldberg, M. D., H. Kilcoyne, H. Cikanek, and A. Mehta, 2013: Joint Polar Satellite System: The United States next generation civilian polar-orbiting environmental satellite system. *J. Geophys. Res. Atmos.*, **118**, 13 463–13 475, doi:10.1002/2013JD020389.

Goody, R. M., and Y. L. Yung, 1989: *Atmospheric Radiation: Theoretical Basis*. 2nd ed. Oxford University Press, 519 pp.

Hilton, F., and Coauthors, 2012: Hyperspectral Earth observation from IASI: Five years of accomplishments. *Bull. Amer. Meteor. Soc.*, **93**, 347–370, doi:10.1175/BAMS-D-11-00027.1.

Inman, R. L., 1969: Computation of temperature at the lifted condensation level. *J. Appl. Meteor.*, **8**, 155–158, doi:10.1175/1520-0450(1969)008<0155:COTATL>2.0.CO;2.

Jackson, C. R., and W. Alpers, 2010: The role of the critical angle in brightness reversals on sunglint images of the sea surface. *J. Geophys. Res.*, **115**, C09019, doi:10.1029/2009JC006037.

Kauth, R. J., and J. L. Penquite, 1967: The probability of clear lines of sight through a cloudy atmosphere. *J. Appl. Meteor.*, **6**, 1005–1017, doi:10.1175/1520-0450(1967)006<1005:TPOCLO>2.0.CO;2.

Kay, S., J. D. Hedley, and S. Lavender, 2009: Sun glint correction of high and low spatial resolution images of aquatic scenes: A review of methods for visible and near-infrared wavelengths. *Remote Sens.*, **1**, 697–730, doi:10.3390/rs1040697.

Knapp, K. R., T. H. Vonder Haar, and Y. J. Kaufman, 2002: Aerosol optical depth retrieval from GOES-8: Uncertainty study and retrieval validation over South America. *J. Geophys. Res.*, **107**, doi:10.1029/2001JD000505.

Larar, A. M., W. L. Smith, D. K. Zhou, X. Liu, H. Revercomb, J. P. Taylor, S. M. Newman, and P. Schlüssel, 2010: IASI spectral radiance validation inter-comparisons: Case study assessment from the JAIVEx field campaign. *Atmos. Chem. Phys.*, **10**, 411–430, doi:10.5194/acp-10-411-2010.

Lawrence, M. G., 2005: The relationship between relative humidity and the dewpoint temperature in moist air: A simple conversion and applications. *Bull. Amer. Meteor. Soc.*, **86**, 225–233, doi:10.1175/BAMS-86-2-225.

Liu, Q., and S. Boukabara, 2014: Community Radiative Transfer Model (CRTM) applications in supporting the Suomi National Polar-orbiting Partnership (SNPP) mission validation and verification. *Remote Sens. Environ.*, **140**, 744–754, doi:10.1016/j.rse.2013.10.011.

Lund, I. A., and M. D. Shanklin, 1972: Photogrammetrically determined cloud-free lines-of-sight through the atmosphere. *J. Appl. Meteor.*, **11**, 773–782, doi:10.1175/1520-0450(1972)011<0773:PDCFLO>2.0.CO;2.

——, and ——, 1973: Universal methods for estimating probabilities of cloud-free lines-of-sight through the atmosphere. *J. Appl. Meteor.*, **12**, 28–35, doi:10.1175/1520-0450(1973)012<0028:UMFEPO>2.0.CO;2.

Maddy, E. S., and Coauthors, 2011: Using *MetOp-A* AVHRR clear-sky measurements to cloud-clear *MetOp-A* IASI column radiances. *J. Atmos. Oceanic Technol.*, **28**, 1104–1116, doi:10.1175/JTECH-D-10-05045.1.

Mandel, J., 1984: *The Statistical Analysis of Experimental Data*. Dover Books on Mathematics, Dover Publications, 432 pp.

Martin, S., 2004: *An Introduction to Ocean Remote Sensing*. 1st ed. Cambridge University Press, 426 pp.

Masuda, K., 2006: Infrared sea surface emissivity including multiple reflection effect for isotropic Gaussian slope distribution model. *Remote Sens. Environ.*, **103**, 488–496, doi:10.1016/j.rse.2006.04.011.

Merchant, C. J., A. R. Harris, E. Maturi, O. Embury, S. N. MacCallum, J. Mittaz, and C. P. Old, 2009: Sea surface temperature estimation from the *Geostationary Operational Environmental Satellite-12* (*GOES-12*). *J. Atmos. Oceanic Technol.*, **26**, 570–581, doi:10.1175/2008JTECHO596.1.

Nalli, N. R., and L. L. Stowe, 2002: Aerosol correction for remotely sensed sea surface temperatures from the National Oceanic and Atmospheric Administration advanced very high resolution radiometer. *J. Geophys. Res.*, **107**, 3172, doi:10.1029/2001JC001162.

——, and W. L. Smith, 2003: Retrieval of ocean and lake surface temperatures from hyperspectral radiance observations. *J. Atmos. Oceanic Technol.*, **20**, 1810–1825, doi:10.1175/1520-0426(2003)020<1810:ROOALS>2.0.CO;2.

——, ——, and B. Huang, 2001: Quasi-specular model for calculating the reflection of atmospheric emitted infrared radiation from a rough water surface. *Appl. Opt.*, **40**, 1343–1353, doi:10.1364/AO.40.001343.

——, and Coauthors, 2006: Ship-based measurements for infrared sensor validation during Aerosol and Ocean Science Expedition 2004. *J. Geophys. Res.*, **111**, D09S04, doi:10.1029/2005JD006385.

——, P. J. Minnett, E. Maddy, W. W. McMillan, and M. D. Goldberg, 2008a: Emissivity and reflection model for calculating unpolarized isotropic water surface leaving radiance in the infrared. 2: Validation using Fourier transform spectrometers. *Appl. Opt.*, **47**, 4649–4671, doi:10.1364/AO.47.004649.

——, ——, and P. van Delst, 2008b: Emissivity and reflection model for calculating unpolarized isotropic water surface leaving radiance in the infrared. 1: Theoretical development and calculations. *Appl. Opt.*, **47**, 3701–3721, doi:10.1364/AO.47.003701.

——, C. D. Barnet, E. S. Maddy, and A. Gambacorta, 2012: On the angular effect of residual clouds and aerosols in clear-sky infrared window radiance observations: Sensitivity analyses. *J. Geophys. Res.*, **117**, D12208, doi:10.1029/2012JD017667.

——, ——, A. Gambacorta, E. S. Maddy, H. Xie, T. S. King, E. Joseph, and V. R. Morris, 2013a: On the angular effect of residual clouds and aerosols in clear-sky infrared window radiance observations 2. Satellite experimental analyses. *J. Geophys. Res. Atmos.*, **118**, 1420–1435, doi:10.1029/2012JD018260.

——, and Coauthors, 2013b: Validation of satellite sounder environmental data records: Application to the Cross-track Infrared Microwave Sounder Suite. *J. Geophys. Res. Atmos.*, **118**, 13 628–13 643, doi:10.1002/2013JD020436.

Newman, S. M., and Coauthors, 2012: The Joint Airborne IASI Validation Experiment: An evaluation of instrument and algorithms. *J. Quant. Spectrosc. Radiat. Transfer*, **113**, 1372–1390, doi:10.1016/j.jqsrt.2012.02.030.

NOAA/NESDIS, 2003: GOES level 3 6km near real time SST 1 hour. PO.DAAC, accessed 3 December 2010, doi:10.5067/GOES3-1HOUR.

Prados, A. I., S. Kondragunta, P. Ciren, and K. R. Knapp, 2007: GOES Aerosol/Smoke Product (GASP) over North America: Comparisons to AERONET and MODIS observations. *J. Geophys. Res.*, **112**, D15201, doi:10.1029/2006JD007968.

Remote Sensing Systems, 2008: GHRSST level 4 mw_ir_OI global foundation sea surface temperature analysis. PO.DAAC, accessed 13 April 2011, doi:10.5067/GHMWI-4FR01.

Smith, W. L., Sr., D. K. Zhou, A. M. Larar, S. A. Mango, H. B. Howell, R. O. Knuteson, H. E. Revercomb, and W. L. Smith Jr., 2005: The NPOESS Airborne Sounding Testbed Interferometer—Remotely sensed surface and atmospheric conditions during CLAMS. *J. Atmos. Sci.*, **62**, 1118–1134, doi:10.1175/JAS3384.1.

——, and Coauthors, 2009: Technical note: Evolution, current capabilities, and future advance in satellite nadir viewing ultra-spectral IR sounding of the lower atmosphere. *Atmos. Chem. Phys.*, **9**, 5563–5574, doi:10.5194/acp-9-5563-2009.

Sokolik, I. N., 2002: The spectral radiative signature of wind-blown mineral dust: Implications for remote sensing in the thermal IR region. *Geophys. Res. Lett.*, **29**, 2154, doi:10.1029/2002GL015910.

Stephens, G. L., 1994: *Remote Sensing of the Lower Atmosphere: An Introduction*. Oxford University Press, 523 pp.

Stull, R. B., 1985: A fair-weather cumulus cloud classification scheme for mixed-layer studies. *J. Climate Appl. Meteor.*, **24**, 49–56, doi:10.1175/1520-0450(1985)024<0049:AFWCCC>2.0.CO;2.

——, 1988: *An Introduction to Boundary Layer Meteorology*. Kluwer Academic Publishers, 666 pp.

Sun, B., A. Reale, D. J. Seidel, and D. C. Hunt, 2010: Comparing radiosonde and cosmic atmospheric profile data to quantify differences among radiosonde types and the effects of imperfect collocation on comparison statistics. *J. Geophys. Res.*, **115**, D23104, doi:10.1029/2010JD014457.

Susskind, J., C. D. Barnet, and J. M. Blaisdell, 2003: Retrieval of atmospheric and surface parameters from AIRS/AMSU/HSB data in the presence of clouds. *IEEE Trans. Geosci. Remote Sens.*, **41**, 390–409, doi:10.1109/TGRS.2002.808236.

Taylor, P. C., and R. G. Ellingson, 2008: A study of the probability of clear line of sight through single-layer cumulus cloud fields in the tropical western Pacific. *J. Atmos. Sci.*, **65**, 3497–3512, doi:10.1175/2008JAS2620.1.

Thomas, G. E., and K. Stamnes, 1999: *Radiative Transfer in the Atmosphere and Ocean*. Cambridge Atmospheric and Space Science, Cambridge University Press, 517 pp.

Thomas, S. M., A. K. Heidinger, and M. J. Pavolonis, 2004: Comparison of NOAA's operational AVHRR-derived cloud amount to other satellite-derived cloud climatologies. *J. Climate*, **17**, 4805–4822, doi:10.1175/JCLI-3242.1.

Weng, F., X. Zou, X. Wang, S. Yang, and M. D. Goldberg, 2012: Introduction to Suomi national polar-orbiting partnership advanced technology microwave sounder for numerical weather prediction and tropical cyclone applications. *J. Geophys. Res.*, **117**, D19112, doi:10.1029/2012JD018144.

WMO, 1956: *International cloud Atlas: Abridged Atlas*. World Meteorological Organization, 62 pp.

——, 1987: *International Cloud Atlas*. Vol. II. World Meteorological Organization WMO-407, 212 pp. [Available online at http://library.wmo.int/pmb_ged/wmo_407_en-v2.pdf.]

Wong, S., E. J. Fetzer, M. Schreier, G. Manipon, E. F. Fishbein, B. H. Kahn, Q. Yue, and F. W. Irion, 2015: Cloud-induced uncertainties in AIRS and ECMWF temperature and specific humidity. *J. Geophys. Res. Atmos.*, **120**, 1880–1901, doi:10.1002/2014JD022440.

Wu, X., and W. L. Smith, 1997: Emissivity of rough sea surface for 8–13μm: Modeling and validation. *Appl. Opt.*, **36**, 2609–2619, doi:10.1364/AO.36.002609.

Yao, Z., J. Li, and J. Li, 2012: Sunglint impact on atmospheric soundings from hyperspectral resolution infrared radiances. *Adv. Atmos. Sci.*, **29**, 455–463, doi:10.1007/s00376-011-1013-8.

Závody, A. M., and A. R. Birks, 2004: Sun glint contamination in ATSR-2 data: Comparison of observations and values calculated from the measured 1.6-μm reflectivities. *J. Atmos. Oceanic Technol.*, **21**, 787–798, doi:10.1175/1520-0426(2004)021<0787:SGCIAD>2.0.CO;2.

Zhang, H., and M. Wang, 2010: Evaluation of sun glint models using MODIS measurements. *J. Quant. Spectrosc. Radiat. Transfer*, **111**, 492–506, doi:10.1016/j.jqsrt.2009.10.001.

Zhao, T. X.-P., P. K. Chan, and A. K. Heidinger, 2013: A global survey of the effect of cloud contamination on the aerosol optical thickness and its long-term trend derived from operational AVHRR satellite observations. *J. Geophys. Res. Atmos.*, **118**, 2849–2857, doi:10.1002/jgrd.50278.